

TOPICAL REVIEW

## Advances in optical recording techniques for non-invasive monitoring of electrophysiological signals

To cite this article: Jiaxin Li *et al* 2024 *J. Phys. D: Appl. Phys.* **57** 493001

View the [article online](#) for updates and enhancements.

### You may also like

- [Etching of Ga<sub>2</sub>O<sub>3</sub>: an important process for device manufacturing](#)

Zhaoying Xi, Zeng Liu, Junpeng Fang et al.

- [Synthesis and recent developments of MXene-based composites for photocatalytic hydrogen production](#)

Yifan Liao, Xinglin Wang, Huajun Gu et al.

- [Negative damping of terahertz plasmons in counter-streaming double-layer two-dimensional electron gases](#)

Shengpeng Yang, Hongyang Guo, Ping Zhang et al.



The ECS United logo features a large green circle containing the text "ECS UNITED" in white, curved along the top edge. Inside the circle, there are three thick, light blue diagonal bars forming a stylized "U" shape.

**ECS** The Electrochemical Society  
Advancing solid state & electrochemical science & technology

**247th ECS Meeting**  
Montréal, Canada  
May 18-22, 2025  
*Palais des Congrès de Montréal*

Showcase your science!

Abstracts due December 6th

## Topical Review

# Advances in optical recording techniques for non-invasive monitoring of electrophysiological signals

Jiaxin Li, He Ding\*, Yongtian Wang and Jian Yang\*

Beijing Engineering Research Center of Mixed Reality and Advanced Display, School of Optics and Photonics, Beijing Institute of Technology, Beijing 100081, People's Republic of China

E-mail: [heding@bit.edu.cn](mailto:heding@bit.edu.cn) and [jyang@bit.edu.cn](mailto:jyang@bit.edu.cn)

Received 18 May 2024, revised 7 August 2024

Accepted for publication 30 August 2024

Published 13 September 2024



### Abstract

The study of electrophysiological signals is crucial for understanding neural functions and physiological processes. Electrophysiological recordings offer direct insights into electrical activity across cellular membranes, aiding in diagnosing and treating neurological disorders. Different from the conventional recording method based on electrical signals and the genetically encoded with fluorescent proteins methods, this review explores label-free mechanisms for optically recording electrophysiological signals: electrochromic materials, surface plasmon resonance (SPR) responses, quantum dots (QDs), and semiconductor-based optoelectronic sensors. The sophistication and limitations of each technology have been discussed, providing insights into potential future directions in this field. Electrochromic materials change optical properties through redox reactions induced by voltages, offering high signal-to-noise ratios and rapid response capabilities. However, these materials have limited biocompatibility and stability. SPR technology modulates signals in response to local changes in electrical potential, achieving high sensitivity. However, challenges such as scattering noise and electro-optic effects still need to be addressed. QDs utilize their photoluminescent properties for high sensitivity and resolution, but concerns about connection efficiency and biocompatibility remain. Semiconductor optoelectronic technologies offer rapid response times, wireless functionality, and integration potential. However, improvements are needed in terms of toxicity, compatibility with biological tissues, and signal amplification and processing. These methods have advantages in neuroscience, medical diagnostics, and biological research, including rapid response, high sensitivity, and label-free monitoring. By combining different optical recording techniques, the performance of voltage imaging can be optimized. In conclusion, interdisciplinary collaboration and innovation are essential for advancing the optical recording of electrophysiological signals and developing diagnostic and therapeutic approaches.

Keywords: optical recording, non-invasive, electrophysiological signals

\* Authors to whom any correspondence should be addressed.

## 1. Introduction

Electrophysiological recordings facilitate the study of diverse cellular activities, spanning from neural networks to myocardial tissues and individual ion channels across cell membranes [1]. Neurons and myocardial cells rely on action potentials to transmit signals and coordinate heart contractions [2, 3]. Electrophysiology has witnessed significant advancements driven by technological progress, improving fidelity and temporal resolution. Over a century ago, Hodgkin and Huxley pioneered the use of glass microelectrodes and silver wires to capture action potentials in giant squid axons [2]. Subsequently, the patch-clamp technique, introduced by Sakmann and Neher, has since become the gold standard for measuring intracellular action potentials [4]. This technique creates a tight seal between the electrode and cell membrane, allowing direct recordings with a high signal-to-noise ratio (SNR) and superior temporal resolution. However, patch-clamp has invasive characteristics that may disrupt the cell membrane, and its complex circuitry design limits the simultaneous recording to one or two cells [5–7]. In contrast, non-invasive extracellular recording methods, such as microelectrode arrays [8], enable simultaneous recordings from multiple neurons [9, 10]. Nanoelectrode arrays have also advanced intracellular recordings by electroporating cell membranes using on-chip nanowires [11]. However, conventional microelectrode arrays have fixed spatial configurations and limited flexibility, highlighting the need for less invasive and more flexible recording techniques like optical electrophysiology.

Optical electrophysiology, which uses light as a sensor, offers several advantages, including spatial flexibility, elimination of electrical connections, and enhanced imaging capabilities [1, 12]. Optical electrophysiology often utilizes fluorescent or calcium indicators [13, 14], such as GCaMP, which are synthesized [15] and integrated into cells [16] to monitor neural activity. These indicators can be customized for specific spectral characteristics and enhanced for greater brightness and accuracy through genetic encoding with fluorescent proteins [17–19]. However, the reliance on elevated calcium ion concentrations during action potential activation with genetically encoded calcium indicators presents challenges, primarily slower response times in data interpretation [13]. Voltage-sensitive dye imaging addresses this issue by incorporating voltage-sensitive dyes into the cell membrane [20, 21], altering their spectral properties in response to voltage fluctuations. Genetically encoded voltage indicators (GEVIs) also assist in the targeted expression of these probes in neural populations [22–25], enabling real-time action potential waveform capture with high sensitivity [26]. However, fluorescence-based voltage recording is limited by photobleaching, which affects membrane depolarization and the velocity of action potential propagation [27], highlighting the need for newer and more robust methods.

Recent advances in the optical recording of electrophysiological signals have been significant, offering increasingly non-invasive techniques resistant to photobleaching or phototoxic effects. This review explores four innovative mechanisms for translating electrical signals into optical readings:

electrochromic materials, surface plasmon resonance (SPR) responses, quantum dots (QDs), and semiconductor-based optoelectronic sensors. Each technology exhibits unique sophistication and limitations, providing insights into potential future directions in this field. This overview may serve as a valuable reference for interdisciplinary applications of optical detection of electrophysiological signals, inspiring ongoing innovation.

## 2. Optical response-based electrophysiological recording with electrochromic materials

Electrochromic materials can alter their optical properties through redox reactions induced by an externally applied voltage. These materials, such as metal–organic frameworks [28], metal oxides [29], and conductive polymers [30], exhibit distinct spectral traits in their reduced and oxidized states. Their applications are diverse, ranging from ‘smart windows’ in aircraft [31] and energy-efficient building facades to paper displays and optical instruments [32]. The unique electrochromic characteristics of these materials provide novel methods for optically sensing cellular electrophysiological signals. This segment delves into the obstacles encountered when utilizing electrochromic properties to detect bioelectrical signals. While metal oxides like tungsten oxide and Prussian blue are commonly employed [33], their biocompatibility and stability in aqueous solutions under physiological conditions are constrained. In contrast, conductive polymers, especially those with  $\pi$ -conjugated structures [34], demonstrate encouraging biocompatibility [35] and mechanical attributes [36]. They are viewed as potential contenders for next-generation electrochromic sensors [37]. Notably, the combination of poly (3,4-ethylene dioxythiophene) (PEDOT) with polystyrene sulfonate (PSS) results in PEDOT:PSS, a versatile conductive polymer. This water-soluble and easily processed blend becomes highly conductive, achieving conductivity exceeding  $1000 \text{ S cm}^{-2}$  after treatment with substances like ethylene glycol or dimethyl sulfoxide [38].

Alfonso *et al* introduce the electrochromic optical recording (ECORE) technique, employing PEDOT:PSS thin films to label-free record cellular action potentials [39]. Figure 1(a) shows that the cells are cultured directly on the PEDOT:PSS films, changing their optical absorption in response to applied voltages and altering their reflectance. To assess the functionality of the PEDOT:PSS film, the UV–Vis absorption spectra at three different voltages are analyzed in figure 1(b). A negative potential of  $-500 \text{ mV}$  resulted in peak absorption ( $\lambda_{\max}$ ) at  $580 \text{ nm}$ , while a positive potential of  $+500 \text{ mV}$  shifted  $\lambda_{\max}$  to  $850 \text{ nm}$  [39]. Figure 1(c) shows the ECORE detected reflectance changes of approximately  $3.0 \times 10^{-3}$  with a root mean square noise below  $2.0 \times 10^{-5}$  in a cell-free environment, indicating a high SNR [39]. Meanwhile, a voltage recording sensitivity of about  $6.7 \mu\text{V}$  with millisecond resolution can be achieved [39]. The ECORE technique successfully recorded spontaneous action potentials from hippocampal neurons and stem cell-derived cardiac myocytes

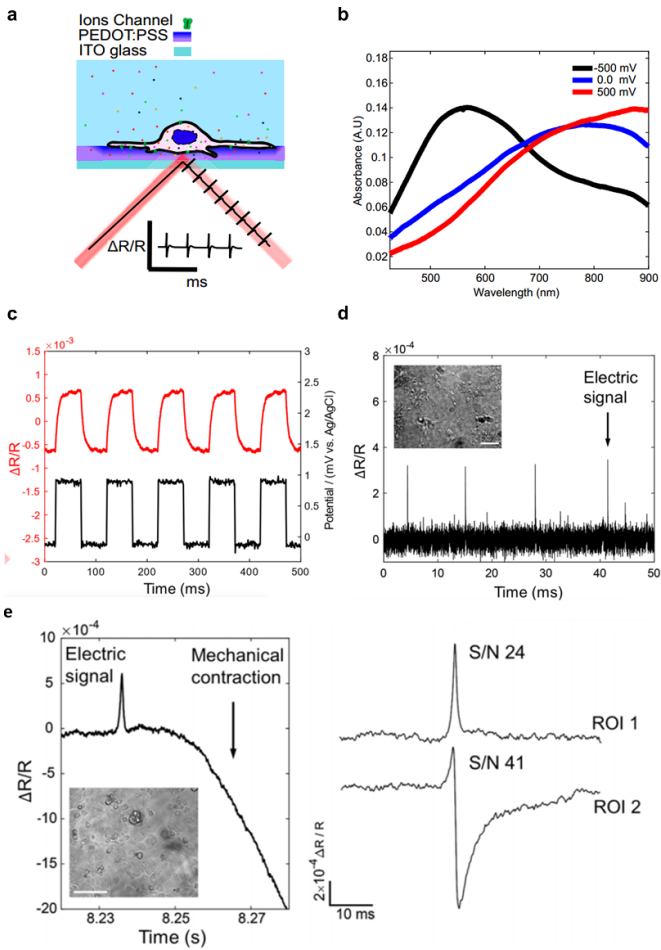


**Figure 1.** (a) Schematic illustration of electrochromic optical recording (ECORE) for label-free optical detection of cellular action potentials using poly(3,4-ethylenedioxythiophene) polystyrene sulfonate (PEDOT:PSS) on an indium tin oxide (ITO)-coated glass substrate. (b) Ultraviolet-visible (UV–Vis) absorption spectra of the PEDOT:PSS film under three different applied voltages. (c) Voltage-modulated fractional reflectivity change ( $\Delta R/R$ ) of the PEDOT: PSS film with a 1 mV square wave applied voltage. (d) ECORE optical recording of spontaneous activity in hippocampal neurons. Inset: bright-field image of cultured hippocampal neurons on a PEDOT film. (e) ECORE visual recording of cardiomyocytes, with a small spike occurring about 15 ms before the onset of mechanical contraction. Inset: bright-field image of stem cell-derived cardiomyocytes cultured on a PEDOT film. Scale bar = 100  $\mu$ m. (Right) the ECORE optical recording of monophasic and biphasic action potential signals of iPSC-derived cardiomyocytes demonstrates a high signal-to-noise ratio. Reprinted with permission from [40]. Copyright (2021) American Chemical Society.

(figures 1(d) and (e)), demonstrating its ability to simultaneously detect electrical and mechanical signals. Electrical signals caused color changes in the electrochromic film, while mechanical signals altered the refractive index of the medium, both affecting the reflectance at the interface. With its dual detection capabilities, ECORE has the potential to advance research in excitation–contraction coupling. Furthermore, this experimental approach detected both single-phase and

biphasic action potentials of stem cell-derived cardiac myocytes without data averaging, achieving a remarkably high SNR of up to 41. Thus, ECORE technique is particularly effective for studying spontaneous electrical activity in individual neurons, which have the distinct advantage of not requiring averaging of multiple recording traces.

Similarly, Yuecheng Zhou *et al* further exploit PEDOT:PSS film with optical absorption in opposite directions at different wavelengths in response to electrical signals [41]. Figure 2(a) shows that this anti-correlated optical absorption significantly enhances signal detection and contrast, effectively distinguishing artifacts from environmental vibrations, cellular mechanical movements, and various noise types [42]. These artifacts and noise typically manifest uniformly across color channels. In the dual-color ECORE detection system with an ultra-sensitive optical platform featuring a prism-coupled total internal reflection setup with differential optoelectronic detection, electrical activity in cells produced signals of opposite polarity, while artifacts and noise are either unrelated or positively correlated. Two detection lasers, emitting at 561 nm and 658 nm, are coupled into the same single-mode optical fiber and focused onto a 25  $\mu$ m spot on the PEDOT:PSS film via a chromatic aberration-corrected prism. The film is fabricated by electropolymerizing 3,4-EDOT monomers with PSS onto an indium tin oxide (ITO) coated glass substrate. Detailed UV–vis spectroscopy measurements of the 90 nm thick film under varied voltages revealed significant shifts, including an absorption peak at approximately 513 nm in its reduced state, which diminished upon oxidation, forming a polaronic band around 700 nm. An isosbestic point near 600 nm indicated minimal absorption change at this wavelength. The differential absorption at 561 nm and 658 nm displayed opposing trends in response to voltage changes from  $-200$  to  $100$  mV (figure 2(b), bottom). Figures 2(c) and (d) detail the total internal reflectance ( $R$ ) and the relative change in reflectance ( $\Delta R/R$ ) under different bias voltages, demonstrating the indirect reflection of changes in optical absorption by the ECORE method. High sensitivity in  $\Delta R/R$  is noted at biases below  $-50$  mV, and both wavelengths responded well at zero bias potential. Dual-color ECORE also successfully detected action potentials in human-induced pluripotent stem cell-derived cardiomyocytes (hiPSC-CM) [41], as electrical signals caused mechanical contractions that affected light reflection, producing complex ECORE signals. This capability enables differentiation between extracellular electrical signals and other disturbances, such as mechanical movements or dust particles. To validate these observations, simultaneous ECORE and patch-clamp recordings are conducted, confirming the accuracy of the action potentials measured by ECORE. Figure 2(f) illustrates the correlation between intracellular and extracellular recordings for the same cell, highlighting consistency with traditional multi-electrode array measurements [11, 43].

The electrochromic recording technique extends beyond responding to cellular action potentials and can also be employed for the broad-spectrum monitoring of bacterial

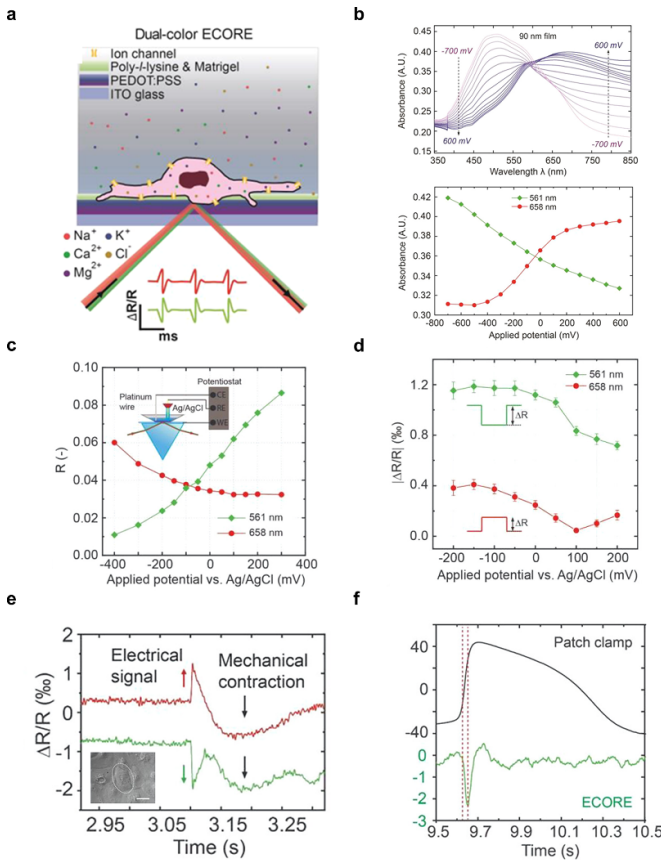


**Figure 2.** (a) Schematic illustration of a dual-color electroChromic recording (ECORE) system utilizing light reflection from PEDOT:PSS thin film, in which two probing lasers at the interface between cultured cells and PEDOT:PSS thin film, and their spectral shifts are triggered by cellular electrical activities. (b) Absorption spectra of PEDOT:PSS films as a function of bias voltage from +600 mV to -700 mV in steps of 100 mV (top), showing opposite changes trend in the green (561 nm) and red (658 nm) spectral regions (bottom). (c) Measurement of reflectance ( $R$ ) of PEDOT:PSS thin film (d) and the absolute value of fractional reflectance change  $|\Delta R/R|$  in response to a 1 mV and 1 Hz applied square-wave potential, respectively, at different bias potentials. (e) ECORE recording traces from the green (561 nm) and red (658 nm) channels. Cell signaling includes electrical signals from cell action potentials (spikes) and mechanical signals (slower waves) from cell contractions. The electrical signal shows opposite polarity in the two channels, while the mechanical contraction and artifact signals show the same polarity. Inset: monolayer of cardiomyocytes cultured on a PEDOT:PSS thin film imaged 11 d after seeding. The cell circled with a dashed line is designated for recording using dual-color ECORE. Scale bar = 50  $\mu$ m. (f) Synchronized recordings of intracellular action potentials from patch clamp and ECORE, where the extracellular spikes are time-aligned with the sharp depolarization phase (indicated by the dashed line). [42] John Wiley & Sons. (Copyright © 2024 WILEY-VCH Verlag GmbH & Co. KGaA, Weinheim).

metabolism at the molecular level. Current *Escherichia coli* (*E. coli*) detection methods, such as bacterial culture [44], enzyme-linked immunosorbent assay [45], and polymerase chain reaction [46], although highly sensitive and specific, often involve lengthy, complex procedures and expensive equipment, limiting their rapid detection capabilities [47].

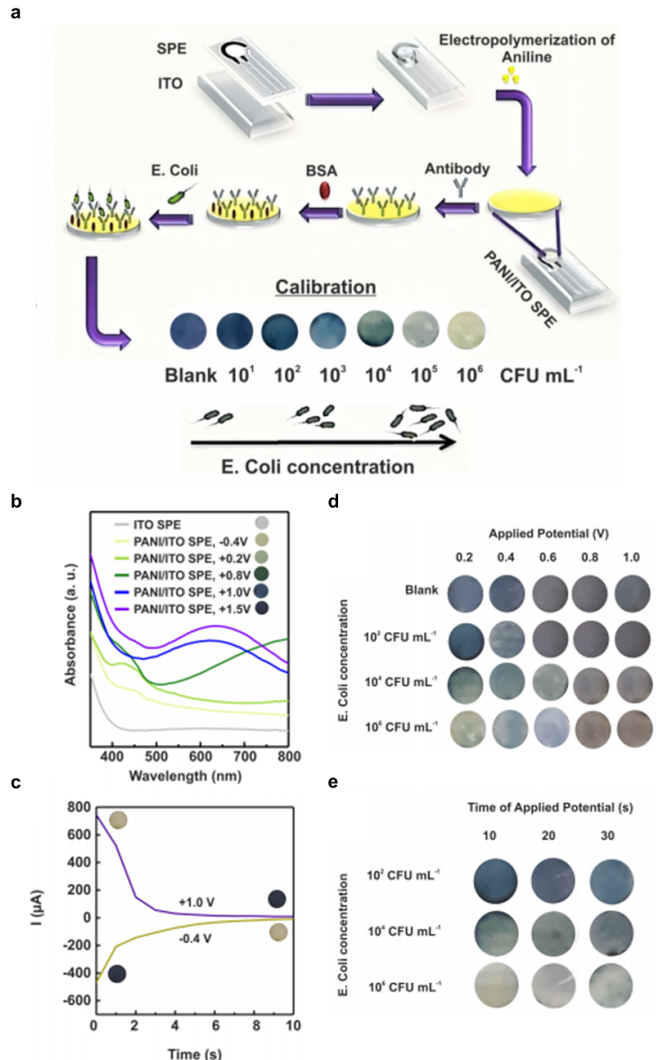


**Figure 3.** (a) Schematic diagram of an electrochromic sensor using electropolymerized polyaniline (PANI) on an indium tin oxide screen-printed electrode (ITO SPE), where the oxidation state changes lead to color changes on the electrode surface. (b) Absorbance spectra of the PANI/ITO thin film under different potential ranges, with peaks at wavelengths of 450 nm and 650 nm representing the leucoemeraldine base and emeraldine, respectively. (c) Chronoamperogram of PANI/ITO in the oxidation and reduction states over time with a fixed potential. (d) Color changes due to applied potential (e) and time duration on signal generation for various *E. coli* concentrations. Reprinted with permission from [51]. Copyright (2019) American Chemical Society.

However, leveraging the principle of redox reactions occurring during bacterial metabolism to induce potential changes, electrochromic probes offer a promising avenue for detection [48–50]. Saba Ranjbar *et al* develop an electrochromic immunosensor that uses polyaniline (PANI) and ITO electrodes to detect *E. coli* in water samples. This sensor leverages specific antibodies for immune recognition, capturing *E. coli* and increasing the electrical resistance on the electrode surface (figure 3(a)). The presence of *E. coli* correlates with distinct absorption spectra at different oxidation states of the PANI film, enhancing the specificity of the sensor (figure 3(b)).

The sensor performance is assessed by recording the time-dependent current of a PANI/ITO Screen-Printed Electrode (SPE) in 0.5 M H<sub>2</sub>SO<sub>4</sub>. This recording tracked the color transition response of PANI under applied voltages of −0.4 V and +1.0 V, revealing a switching time of 1.25 s between the complete reduction and oxidation of the PANI film, with an average switching time of about 0.4 s among the three PANI oxidation–reduction states (figure 3(c)). Additional experiments evaluated the signal response to varying concentrations of *E. coli* under different voltages and durations (figures 3(d) and (e)). These results showed that a minimum applied voltage of 0.2 V is insufficient to significantly modify the electrochromic characteristics of PANI, leading to reduced sensitivity. Nonetheless, the sensor successfully detected *E. coli* in water samples, confirming its potential as an effective tool for analyzing bacterial contaminants. The electrochromic immunosensor enables visual detection without the need for expensive equipment, providing a user-friendly, multicolor display. This enhances its practicality compared to traditional optical sensors due to the acute sensitivity to color changes of the human eye, making it an economical and straightforward solution for monitoring various bacteria and viruses in diverse environments, including clinical, environmental, and food settings. Future research should focus on improving detection sensitivity and reducing incubation times to achieve more effective real-time measurements [51].

Wu *et al* develop a sensor to enhance the spectral response resolution using a water-soluble electrochromic polymer [52]. This polymer, a copolymer of PPE (3,4-propylenedioxythiophene-alt-3,4-ethylenedioxythiophene), detects metabolically active bacteria. PPE, traditionally used in electrochromic devices for color control, has a low oxidation potential, allowing it to naturally oxidize to its oxidized form (ox-PPE) in the presence of environmental oxygen. Metabolically active bacteria then reduce this oxidized form, primarily through reactions triggered by extracellular metabolites rather than direct bacterial contact. The reduction process is particularly sensitive to cysteine and GSH, providing high sensitivity and specificity. The electrochromic properties of ox-PPE enable rapid and convenient detection of bacterial activity, allowing modulation of PPE color through electrochemical reactions (figure 4(a)). As illustrated in figure 4(b), upon electrochemical oxidation, the PPE film transitions from a blue state at −600 mV in the visible spectrum to a bleached state at 310 mV in the near-infrared range [52]. The absorption peaks shift from around 600 nm for neutral PPE to beyond 1500 nm for fully oxidized bipolaron bands, with partial oxidation producing polarons near 1000 nm [53, 54]. Due to its low oxidation potential, PPE primarily forms stable and minimally cytotoxic bipolarons in aqueous solutions (pH = 7.4). This stability, along with the water solubility of ox-PPE, enhances its interaction with analytes in solution. Figure 4(c) shows the experimental results and demonstrates the effectiveness of ox-PPE as a colorimetric sensor, with absorbance spectroscopy improving detection sensitivity. As depicted in figure 4(d), the sensor can distinguish bacterial concentrations as low as 10<sup>4</sup> cells ml<sup>−1</sup>, making it suitable for clinical applications. The sensor's accuracy is verified

by monitoring *E. coli* growth through the optical density (O.D.) at 600 nm as a control (figure 4(e)). With a reaction time of 30 min, it significantly outperforms traditional culture-based methods [55], offering a practical advantage in clinical settings [56]. The electrochromic immunosensor enables visual detection without expensive equipment, utilizing the sensitivity of the human eyes to color changes. Future research will focus on improving the detection sensitivity and reducing incubation times for real-time applications. Furthermore, the inclusion of electrochromic transition metal oxides could enhance the visual detection capabilities of these sensors.

Thus, the electrochromic technology has promising applications in areas such as recording cellular action potentials and monitoring bacterial metabolism. Compared to traditional methods, electrochromic technology offers the advantages of simplicity, cost-effectiveness, and visual detection capabilities, making it significant in clinical, environmental, and food supply fields [40]. Future research will focus on enhancing detection sensitivity, reducing incubation times before detection, and improving the visual detection capabilities of electrochromic sensors to meet real-time monitoring demands.

### 3. Optically-responsive SPR for electrophysiological recording

SPR is an optical sensing technique utilized in biosensors, relying on the oscillation of electrons within metal nanostructures [57]. These oscillations are influenced by various factors, including the size, shape, composition, dielectric properties, and surrounding environment of the nanostructures [58–62]. SPR can be categorized into two types based on the mode of transmission: localized SPR (LSPR) and propagating surface plasmon polariton (SPP) [57]. LSPR occurs when the dimensions of metal nanostructures are smaller than the wavelength of incident light, leading to localized electron oscillations. This localization makes LSPR highly sensitive to changes in the refractive index of the adjacent medium, making it ideal for the development of colorimetric plasmonic sensors. Additionally, LSPR enhances the sensitivity of various optical processes, such as fluorescence, Raman scattering, and infrared absorption [57]. Conversely, SPP involves the propagation of electron charge oscillations along the surfaces of thin metal films. This propagation interacts with the surrounding medium and can influence sensor signals over longer distances, typically up to about 200 nm [57]. The extended reach of SPP is beneficial for applications like plasmon-enhanced fluorescence and surface-enhanced Raman scattering (SERS), which improve detection capabilities and practicality.

SPRs in the visible/near-infrared wavelength range are of particular interest because there is favorable optical confinement at these wavelengths, and they may become a major component in the next generation of biosensors [63]. Many metallic nanostructures have been developed as signal amplifiers and sensors for sensitive optical sensing by utilizing LSPR [57, 64, 65]. It is crucial to apply the fundamental physical

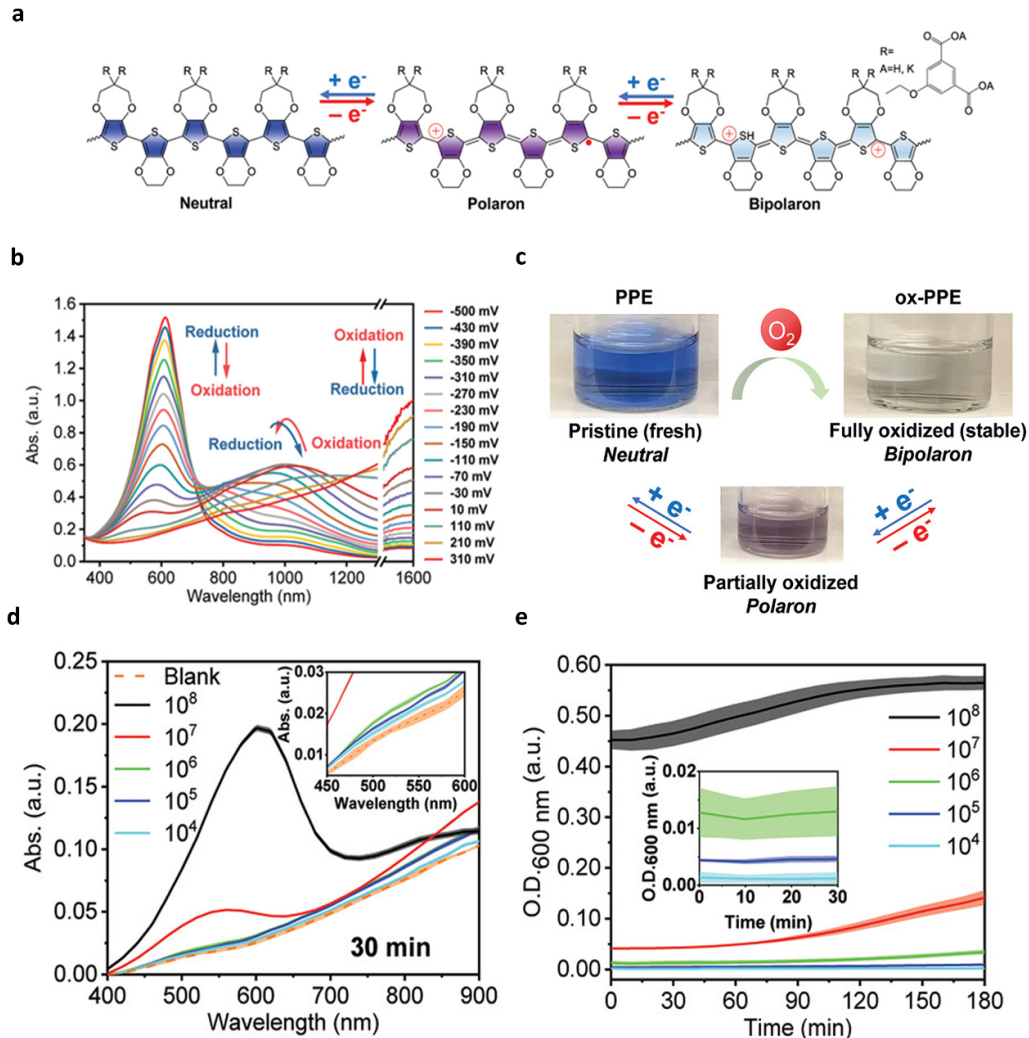


**Figure 4.** (a) Schematic illustration of an aqueous soluble electrochromic poly(3,4-propylenedioxythiophene-alt-3,4-ethylenedioxythiophene) copolymer (PPE) in three different oxidation states and their conversion through electrochemical reactions. (b) Spectroelectrochemistry of PPE in response to electrochemical oxidation upon applied voltages. (c) Photographs of PPE aqueous solutions in the neutral state (treated with  $\text{N}_2\text{H}_4$  reducing agent) and in the polaron/bipolaron (ox-PPE) state following ambient oxygen oxidation. (d) Absorption spectra of ox-PPE to various concentrations of *E. coli* in a 30 min reaction period. (e) Growth of *E. coli* monitored by optical density (O.D.) at a wavelength of 600 nm. [52] John Wiley & Sons. (Copyright © 2020 WILEY-VCH Verlag GmbH & Co. KGaA, Weinheim).

principles of plasmonic enhancement to guide sensor design, aiming to achieve maximized signal transduction and amplification. Figure 5(a) shows that LSPR occurs when the size of metal nanoparticles is smaller than the wavelength of the incident light, causing electrons to oscillate in phase and leading to increased absorption and scattering cross-sections and enhanced local electromagnetic fields. Figure 5(b) shows that nanoparticles smaller than 15 nm primarily exhibit absorption, making them useful in detecting molecules or biomolecules. On the other hand, figure 5(c) shows that nanoparticles larger than 15 nm mainly have scattering properties, which are advantageous for SERS. These size-dependent phenomena are important for developing sensitive and selective optical sensors, as they affect the interaction of metal nanostructures and light [66]. However, challenges remain due to the high electron density in metals, resulting in weak electro-optic effects associated with non-Faradaic capacitance

[67]. Additionally, the use of plasmonic nanostructures for optical field measurements is often complicated by scattered particle noise [67]. Despite significant research efforts, creating optical probes that can detect local electric field dynamics with high sensitivity and spatiotemporal resolution remains a challenge.

Zhang *et al* develop an optical sensing technology that utilized localized SPR (LSPR) to detect mammalian brain cell activity [68]. This research involved using optical methods to detect changes in the SPR modes of planar gold nanoparticle arrays, which are influenced by neuronal potentials. Hippocampal neurons are cultured directly on these nanoparticle arrays, enabling the detection of individual transient signals at the cellular level. The experimental findings are consistent with theoretical calculations by using the Drude and Stern models [68]. For the experiments, neuron-plasmon samples are moved from a culture environment to a solution of

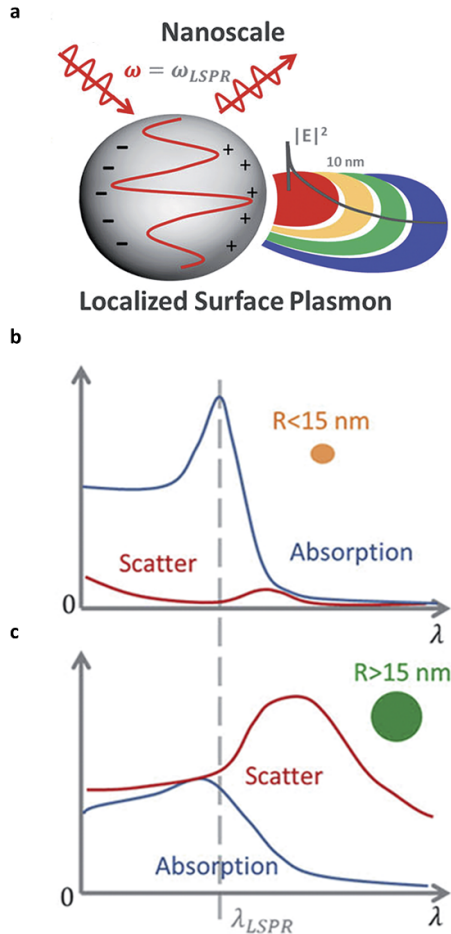


**Figure 5.** (a) Schematic diagram of localized surface plasmon resonance with a metal nanoparticle smaller than the incident wavelength and the generation of in-phase electron oscillations. (b) Absorption dominates, and the absorption cross-section is large for particles smaller than 15 nm. (c) Scattering cross-section dominates for nanoparticles larger than 15 nm. Reproduced from [65]. CC BY 4.0.

artificial cerebrospinal fluid containing essential ions and glucose. Neurons are stimulated to activity by injecting 50  $\mu\text{M}$  of glutamate, causing rapid spikes in membrane potential. These spikes are observed using a  $40\times$  water-immersion objective lens focusing 850 nm laser light onto the neurons (figure 6(a)). A CCD camera captured the process, recording the forward-scattering light signal emitted by the neurons without averaging, using a low-noise preamplifier connected to an oscilloscope. Figure 6(c) displays the differential scattering signal ( $\Delta S/S$ ) of the nanoparticle template at various voltages. The AC signal ( $\Delta S$ ) is captured using a lock-in amplifier, while the DC signal (approximately 250 mV) is monitored via an oscilloscope. This model proposed by McIntyre [69] and Lioubimov [70], which explains resonance changes in gold films under oscillating potentials, is used to describe the changes in scattering signals. The scattering signal increased linearly with the applied voltage at a rate of  $2.8 \times 10^{-6} \text{ V}^{-1}$  (at the detection wavelength of 850 nm), aligning with theoretical expectations (figure 6(d)). A previously used model

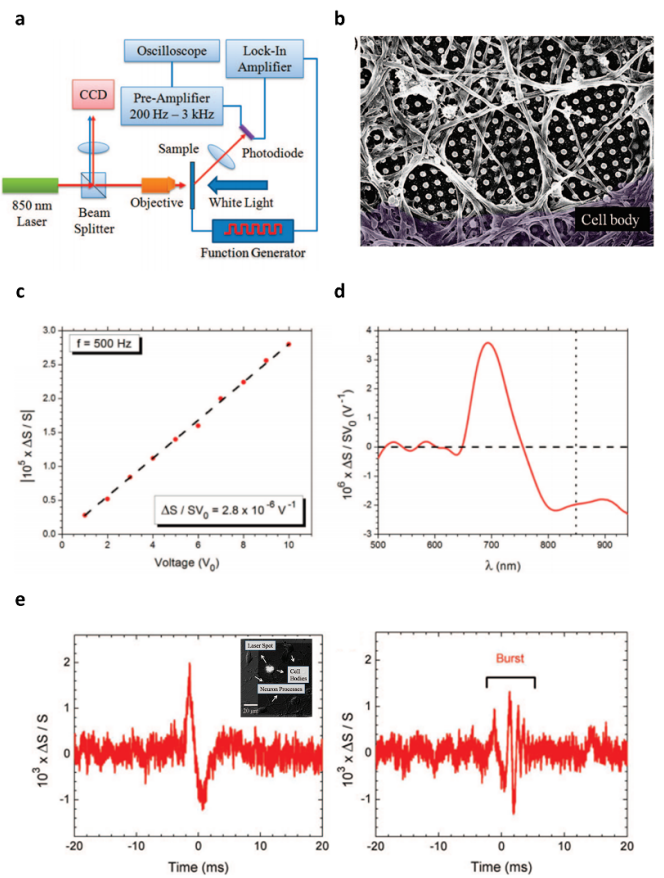


**Figure 6.** (a) schematic illustrates the overall setup for optical recording of brain cell activity. White light aligns neural samples onto a CCD camera. Scattered signals from the naked plasma samples are then directed into a lock-in amplifier. For real-time neural measurements, signals first pass through a low-noise preamplifier before being fed into an oscilloscope. This oscilloscope operates within a frequency range of 200 Hz–3 kHz. (b) SEM image of a hippocampal neuron cultured on the template after 14 d *in vitro*. (c) The generated differential scattering signals under an electric field with a modulation frequency of 500 Hz. The dashed line represents the linear fitting of the experimental data (dots). (d) Differential scattering signal per applied voltage. (e) Differential scattering signals from the plasmon/neuron sample represent single spike activity (left) and a burst of spikes (right), each trace being recorded from a single neural cell. Reprinted with permission from [68]. Copyright (2009) American Chemical Society.

to describe changes in SPR across oscillating potentials in gold films provided estimates that closely matched the experimentally obtained data. Further analysis included a scanning electron microscope (SEM) image of isolated hippocampal neurons cultured on a plasma template, as shown in figure 6(b). The SEM image illustrated the physical arrangement of neurons on the template post-cell dehydration. Before glutamate injection, minimal changes in the scattering signal are noted, but significant spike activity is observed afterward. Figure 6(e) demonstrates the extracellular electrode-like single and series of spikes from two different neurons, confirming the method's effectiveness. The measured scattering changes induced by neuronal spikes are greater than

those caused by inherent birefringence changes in the neurons, indicating superior sensitivity and temporal resolution comparable to voltage-sensitive fluorescent dyes [68]. This study demonstrated the real-time detection of neuronal spikes through shifts in LSPR in gold nanoparticle optical probes and highlighted the potential applications of metal nanoparticles in all-optical recordings within the body. The scalability of this technique suggests its applicability for monitoring multiple neurons in neural microcircuits, depending on the geometric configuration of the plasmon probe array, thus opening new possibilities for non-invasive neural monitoring technologies.

Ahsan Habib *et al* introduce the electro-plasmonic nanoantenna in 2019, in which the optical field probe surpassed existing electro-optic field reporters regarding photon counting and field sensitivity. This nanoantenna facilitated non-invasive optical measurements of electric activity in hiPSC-CM with lower light intensity ( $11 \text{ mW mm}^{-2}$ ) compared to traditional fluorescence voltage probes [14]. It achieved a field sensitivity enhancement of approximately 3250 times that of conventional plasma nanoantennas [68]. The structure of the nanoantenna, with a height of 45 nm and a diameter of 90 nm, is arranged in a submicron periodic pattern and incorporated PEDOT: PSS, significantly improving its electric field measurement capabilities over the original plasma design [71]. Figure 7(a) illustrates the experimental setup for dark-field transmission measurements, using a  $20\times$  objective lens and a spectrometer with a 50 ms integration time to continuously collect far-field scattering signals. Three-dimensional finite-difference time-domain (FDTD) simulations demonstrated that the nanoantenna could confine electromagnetic fields within a narrow region, enhancing light and matter interactions (figure 7(b)). Employing concepts from radiofrequency antenna design, the research team explored the far-field response of the nanoantenna to local field dynamics, supporting interpretations within the framework of optical path theory [72, 73]. These findings are visualized in figure 7(c), which shows a wavelength-dependent electric response indicating a redshift in the far-field plasma response corresponding to the electrochromic transition from a doped to a de-doped state. Figure 7(d) illustrates the temporal optical response of the nanoantenna to a periodic square wave ( $-500$  to  $+500$  mV, 100 Hz). The response time, determined to be 191 ms by fitting the decay function, demonstrates its suitability for high time-resolution electrophysiological signal detection. During the measurement of electrical activity in induced cardiomyocytes, spontaneous emission led to increased light scattering, consistent with prior photoelectrochemical measurements (figure 7(e), red curve). Control experiments on iCMs cultured without the nanoantenna confirmed the absence of far-field light signals corresponding to cell discharge events, validating the accuracy of the measurements (figure 7(e), blue curve). This study on electro-plasmonic nanoantennas highlights significant advancements in optical field measurements [71], offering high sensitivity and abundant photon counts. Future research could further enhance these technologies through optimization and the introduction of new materials, potentially improving optical capabilities for deep tissue imaging. However, further investigations are needed

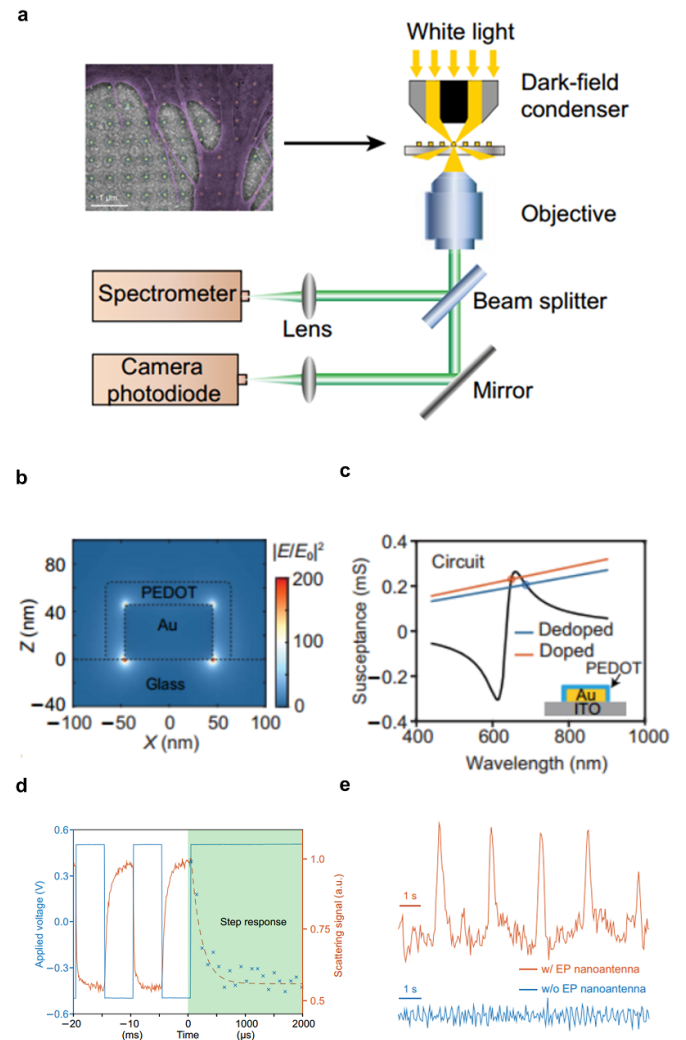


**Figure 7.** (a) Schematic diagram of the transmission dark-field measurement setup designed for optical recording of electrogenic activity. Inset: a false-color scanning electron micrograph of hiPSC-derived iCMs (colored purple) cultured on an electroplasmonic nanoantenna array. (b) Side view of near-field enhancement  $|E/E_0|^2$  along the pristine nanoantenna in FDTD simulations leads to strong confinement of the light within the 20 nm-thick electrochromic layer. (c) Susceptances of the gold nanoantenna and the PEDOT:PSS load for doped (red) and developed states (blue). (d) Temporal optical response of the electro-plasmonic nanoantenna (red curve) for potential steps in a square wave voltage (blue curve) between  $-500$  mV and 500 mV with a residence time of 5 ms. (e) Optical detection of differential scattering signal in response to the electrogenic activity of a network of cardiomyocyte cells, in which electrogenic activity of iCMs is obtained from substrates with electro-plasmonic nanoantennas (red curve) and without (blue curve). From [71]. Reprinted with permission from AAAS.

to understand the long-term biocompatibility and safety of these nanoantennas *in vivo* [71]. In the context of neuroscientific research, the need to understand how the human brain executes complex functions remains a significant challenge. It requires advancing technologies for recording brain activity with high spatiotemporal resolution and large-scale reusability. Traditional methods, such as electrode arrays, are

limited by complex wiring, bandwidth constraints, and the need for invasive neurosurgical procedures. These limitations underscore the urgent need for innovations like the electroplasmonic nanoantenna in non-invasive brain activity monitoring, which could revolutionize our approach to understanding neuronal communication across various brain regions [74–76].

For the issues mentioned above, Hardy *et al* introduce Neuro-SWARM<sup>3</sup>, a nanoparticle probe system utilizing near-infrared light (NIR-II, 1000–1700 nm) for the wireless remote detection of internal bioelectric signals [77]. Neuro-SWARM<sup>3</sup> presents several advantages, including directly reading signals through the near-infrared window, thus eliminating the need for invasive surgeries. Its compact size enables the delivery of the system to various brain regions without the need for neurosurgical intervention. Neuro-SWARM<sup>3</sup> converts signals directly at the plasma level, bypassing the need for front-end signal processing and overcoming limitations related to electrode size and electronic bandwidth. The probes, with a diameter of less than 200 nm and coated with lipids [77], are designed to cross the blood-brain barrier when administered intravenously. Figure 8(a) illustrates these probes binding to cell membranes via surface-functionalized proteins [78]. In practical applications, Neuro-SWARM<sup>3</sup> detects neural activity by monitoring far-field scattering signals that correspond to transient electric field oscillations generated by neural networks during neuron firing events. These events, particularly driven by sodium ( $\text{Na}^+$ ) and potassium ( $\text{K}^+$ ) ion currents, result in significant fluctuations in membrane potential. Figure 8(b) depicts how these fluctuations generate strong transient electric fields and significantly modulate the reverse scattering signals from Neuro-SWARM<sup>3</sup>, thereby facilitating far-field detection. Figure 8(c) compares the differential signals from Neuro-SWARM<sup>3</sup> against simulated electrophysiological recordings using CdSe QDs. Neuro-SWARM<sup>3</sup> significantly outperforms QDs, offering a high-photon-count alternative to GEVIs [79] with an enhancement of at least four orders of magnitude in photon count measurements (left axis) at an intensity of  $10 \text{ mW mm}^{-2}$ . This exceptional performance, evidenced by an extraordinarily high SNR ( $\text{SNR} \sim 10^3$ ), paves the way for new possibilities in brain-machine interfaces and highlights the immense potential of SPR in optical sensing. This innovative approach could revolutionize the field of neural monitoring, providing a non-invasive, highly sensitive tool for the real-time observation of brain activity [77].

These studies highlight the crucial role of SPR technology in optical neuroscience research, introducing innovative methods for monitoring neural activity. From the initial use of plasmonic-enhanced optical sensors to the advanced application of wireless remote detection via near-infrared light, the development of these techniques opens new pathways for understanding neuronal communication and functional dynamics across various brain regions. Enhancing sensor sensitivity and spatiotemporal resolution is essential for achieving more precise and comprehensive monitoring of neural

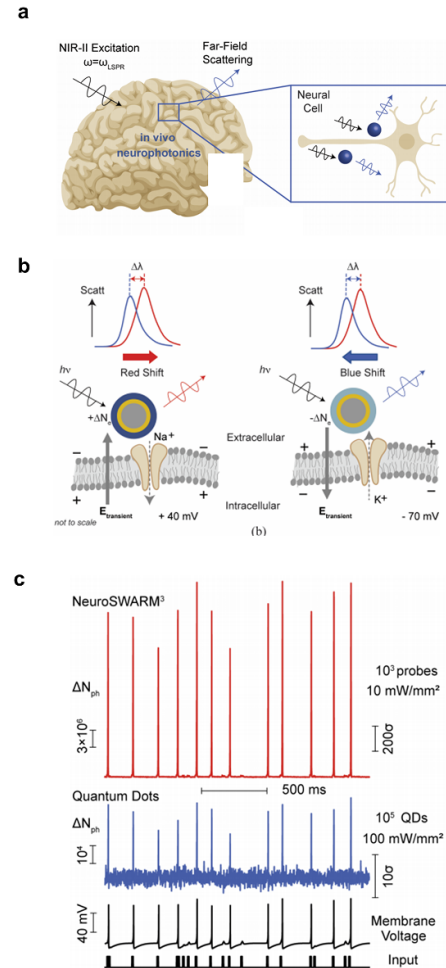


**Figure 8.** (a) Schematic diagram of remotely detecting neuronal activity based on neurophotonic solution-dispersible wireless activity reporter for massively multiplexed measurements (NeuroSWARM<sup>3</sup>). (b) Illustration of the high transient electric field generated by cell depolarization (spiking) leading to spectral changes of increased light scattering and red shifting of the electro-plasmonic (electrochromic-plasmonic) nanoantenna. (c) Simulated electrophysiological recordings with NeuroSWARM<sup>3</sup> and quantum dots (QDs). The input and resulting membrane voltage are represented in black at the bottom of the graph. The differential scattering signal, detected by  $10^3$  NeuroSWARM<sup>3</sup> probes (top red line), assumes a light intensity of  $10 \text{ mW mm}^{-2}$  at a wavelength of 1050 nm. The differential fluorescence signal, obtained from  $10^5$  CdSe quantum dots under an illumination intensity of  $100 \text{ mW mm}^{-2}$  (middle blue line), assumes a maximum extracellular field of  $3 \text{ mV nm}^{-1}$  for this experiment. The photon count for the differential signal and the standard deviation due to shot noise are noted on the left and right scale bars, respectively. [78] John Wiley & Sons. (Copyright © 2024 WILEY-VCH Verlag GmbH & Co. KGaA, Weinheim).

activity. Moreover, investigating a broader range of materials and design strategies to improve sensor performance and deepen penetration into brain structures could lead to significant advancements in diagnosing and treating neurological disorders.

#### 4. Spectral response-driven electrophysiological recording with QDs

QDs are increasingly recognized as valuable tools for addressing the challenges of real-time optical voltage imaging in neuroscience research. Their exceptional photoluminescent properties can significantly enhance monitoring sensitivity [80–82]. QDs offer several advantages for this application: they possess a high photoluminescence (PL) quantum yield [83], which facilitates two-photon excitation using lower laser power, and their resistance to photobleaching prolongs their usability in experimental settings. This durability is especially beneficial for addressing issues like tissue autofluorescence and scattering, which are common in deep-tissue imaging [84]. Currently, methods for measuring electric fields with QDs mainly revolve around three concepts. The first involves the quantum confined Stark effect (QCSE), where the electric field within the lipid membrane bilayer impacts the PL of QDs, leading to a redshift and broadening of the spectrum and a reduction in PL intensity (figure 9(a)). The other two methods involve Förster resonance energy transfer (FRET) or electron transfer (ET) to modulate the PL intensity of QDs. The FRET-based sensing approach utilizes dye–receptor translocation: an impermeable donor fluorophore on the extracellular membrane surface interacts with an acceptor dye within the lipid bilayer [85, 86]. As illustrated in figure 9(b), upon cell depolarization, the dye shifts to the inner leaflet of the cell surface, reducing FRET efficiency and enhancing donor PL. This allows for real-time tracking and visualization of neuronal activity. Photo-induced ET (PET), utilized as a cellular voltage sensor, involves the transfer of electrons from a donor through molecular wires attached to a fluorophore embedded in the cell membrane [87]. During depolarization, the ability of the electron donor to quench the fluorophore is disrupted, altering ET rates. This modification enables the real-time detection and recording of cellular depolarization events (figure 9(c)).

However, connecting QDs to neuronal membranes is a non-trivial task. Among them, custom ligands [80] or peptides [82] to target QDs to neurons is critical in achieving QD voltage sensing/imaging. Nag *et al* conducted a study on the use of QDs for visualizing changes in membrane potential in living cells and *in vivo* in mouse brains [88]. The system used a 605 nm-emitting QD connected to a C<sub>60</sub> fullerene electron acceptor through a membrane-inserting peptide (figure 10(a)). Under resting conditions, photoexcited QDs engaged in ET with the C<sub>60</sub> at a basal rate, resulting in moderate PL quenching. During depolarization, ET rates increased, leading to further quenching (figures 10(b) and (c)). For the *in vivo* application of this technology, a QD-peptide-C<sub>60</sub> bioconjugate is injected into the cortex, and dual-pole tungsten electrodes are used for simultaneous imaging and stimulation. This setup allowed for the observation of significant, reversible modulations in PL, with consistent responses across experiments (figures 10(d)–(f)). Compared to traditional voltage-sensitive dyes like RH-795 and RH-1691, the QD-based probe showed a dynamic response of 20–40 times greater under similar experimental conditions [89], indicating superior sensitivity and

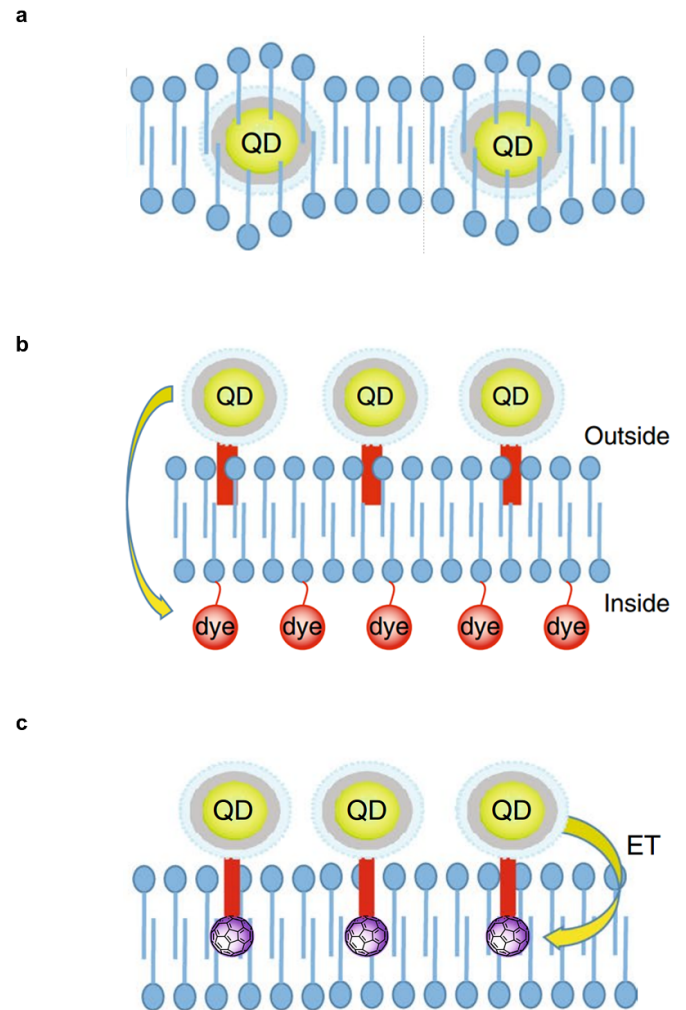


**Figure 9.** (a) Schematic diagram of quantum dot (QD) photophysical properties for three different positions with mechanisms of QDs in a membrane bilayer that can measure the electric field directly, (b) QD geometry that allows measurement of the electric field using PL modulation facilitated by electric field-dependent FRET, (c) and electric field-sensitive electron transfer (ET) mechanisms.

temporal resolution. Incorporating QDs into neuronal voltage sensing represents a significant advancement in monitoring neural activity, offering enhanced sensitivity and stability for long-term studies in complex biological environments. This breakthrough represents the potential to improve the ability to study and understand neural dynamics greatly.

To evaluate the potential of QDs in cellular systems, measurements in an aqueous ionic environment are required [90]. However, the fabrication of commonly used capacitor structures poses challenges, as it requires multiple cycles of dielectric deposition, and under high-energy conditions, it may damage the QDs within the device [79]. Therefore, there is a need for a platform that can quantitatively evaluate the voltage-sensing capability of QDs in a high-throughput, reproducible, and non-destructive manner [79]. Caglar *et al* develop a platform for assessing the voltage-sensing capabilities of

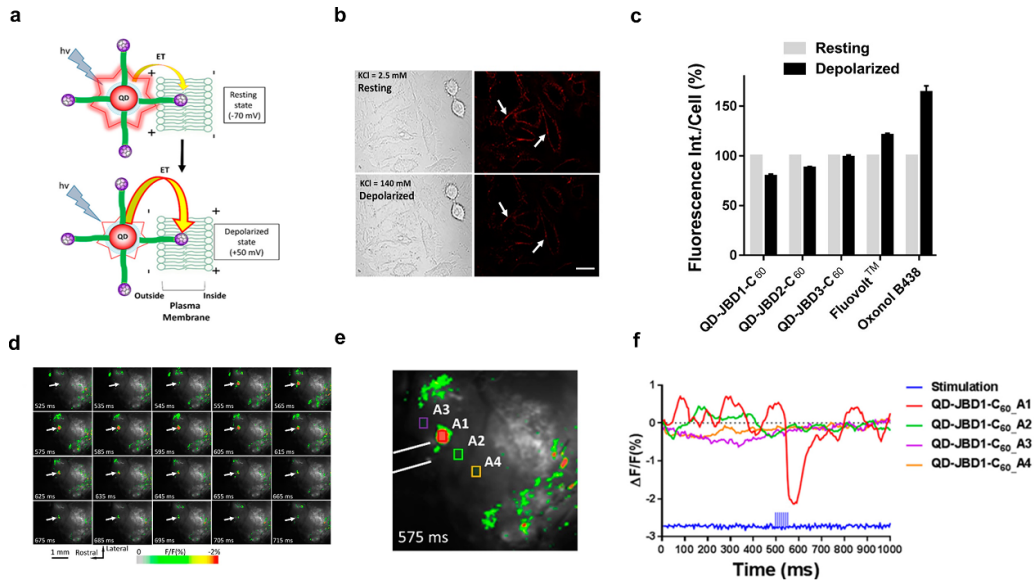


**Figure 10.** (a) Schematic diagrams of the photoluminescence response of the quantum dot peptide fullerene ( $C_{60}$ ) electron transfer (ET)-based nanobioconjugate for the visualization of membrane potential in living cells, in which QD emission is modulated with resting potential and depolarization states via ET process. (b) Differential interference contrast (DIC) and confocal fluorescence images of membrane potential changes in HeLa cell monolayers labeled with QD-peptide- $C_{60}$  probe bioconjugates before (top) and after (bottom) depolarization with KCl solution. (c) Comparison of the fluorescence intensity between resting (2.5 mM KCl, gray bar) and depolarized (140 mM KCl, black bar) membrane. (d) *In vivo* optical imaging of the mouse cortex injected with QD-JBD1- $C_{60}$  conjugates during electrical stimulation, and the red points indicate ROI A1. (e) Fluorescence response of four ROIs with an acquisition frame of 575 ms. (f) Time-resolved fluorescence response of the four ROIs with the averaged response of 50 trials. Reprinted with permission from [88]. Copyright (2017) American Chemical Society.

QDs in an aqueous ion environment [91]. Given that conventional capacitor structures can damage QDs, this new platform enables non-destructive PL measurements. As shown in figure 11(a), the device comprises an ITO-coated glass slide with a thin layer of dielectric (approximately 300 nm of  $Ta_2O_5$ ) to prevent charge transfer to the QDs. These dots are positioned between the working electrode and an electrolyte (potassium nitrate solution) within an electrochemical cell setup. Platinum electrodes serve as the working and reference electrodes, while a silver electrode connected to the ITO surface acts as the counter electrode. A potentiostat regulates the configuration to maintain desired voltage levels. Integrating the device into an inverted fluorescence microscope setup facilitates the excitation of QDs with a 532 nm laser and the capture of emitted light through the ITO layer into a fiber optic spectrometer. This setup permits the simultaneous monitoring of PL responses under controlled voltage conditions. Finite element simulations have revealed that the region above the QDs on the dielectric surface experiences the strongest electric field, with intensity varying according to the salt concentration in the electrolyte (figure 11(b)). Both types of QDs exhibit significant modulation of their PL under applied electric fields, with CdSe/CdS dots showing up to 60% quenching (figure 11(c), upper image) and InP/ZnS dots achieving around 70% under similar conditions (bottom image). Figure 11(d) shows the voltage waveforms for CdSe/CdS and InP/ZnS dots, as well as the axonal dye, under a 1 Hz sine wave. The PL response closely follows the voltage waveform in all cases, without any noticeable delay. In subsequent

experiments, QDs are injected into the central nervous system of early-stage embryonic cells of African clawed frogs. After culturing the cells to differentiate into neurons, neuronal membrane depolarization is induced, and changes in the PL of the QDs are observed (figure 11(e)). The rapid depolarization, bringing the membrane potential close to 0 mV from  $-70$  mV, corresponded with an increase in QD brightness—a clear indication of successful voltage sensing (figure 11(f)). This study demonstrates the robust response of QDs to voltage changes and their potential as powerful tools in neuroscience research and other fields requiring precise voltage monitoring.

The primary aim of a voltage indicator is to assess and visualize changes in local membrane potential accurately. Traditional single-point detection methods have expanded to include wide-field PL imaging techniques [91]. In a notable study, QDs are injected into the axon terminals of retinal ganglion cells (RGCs) in African clawed frogs, alongside a calcium indicator called jGCaMP7f. This setup allowed for the simultaneous monitoring of PL changes in both the QDs and the calcium indicator during osmotic shock-induced membrane depolarization. Figure 11(g) illustrates the effectiveness of this dual-channel approach. The left image depicts wide-field epi-fluorescence excitation/detection, capturing fluorescence images of PL responses to osmotic shock-induced membrane depolarization. The right image provides details of the changes in PL intensity over time for both the QDs and the calcium indicator dye. Notably, the PL changes in the QDs consistently exceeded those observed in the calcium dye, with

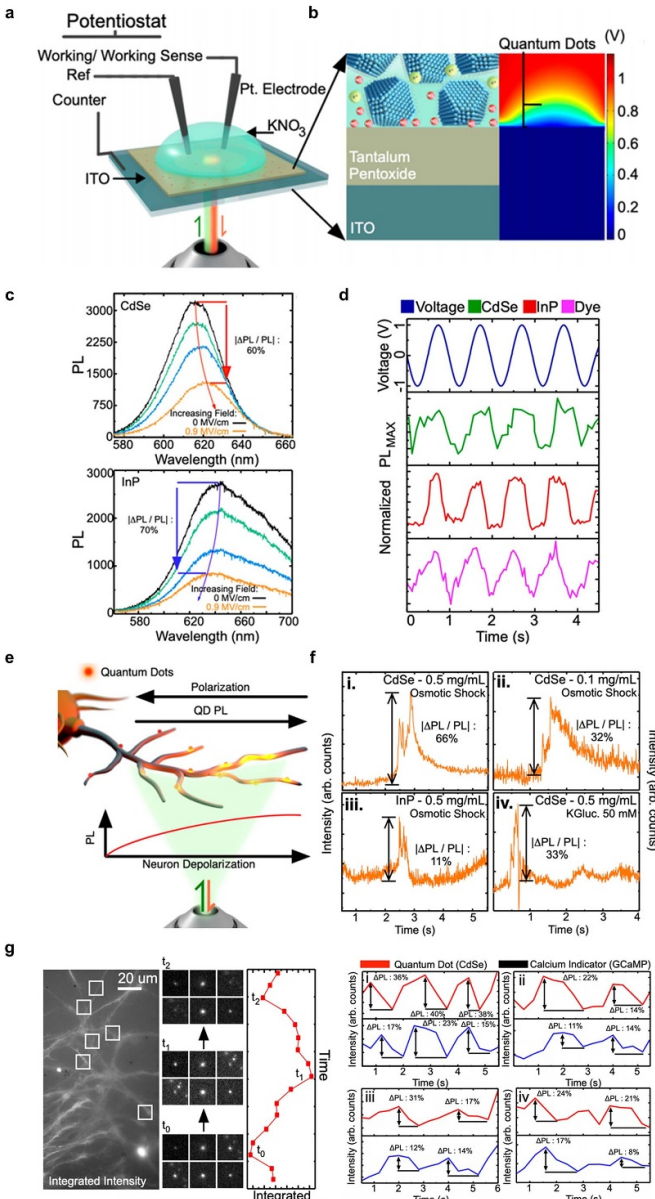


**Figure 11.** (a) Schematic diagram of an electrochemical setup used to apply voltage and monitor photoluminescence (PL) from quantum dots, in which the sample is excited with a 532 nm laser ( $\sim 1 \mu\text{m}$  beam size) and the emission is collected through the ITO back surface. (b) Schematic diagram of the samples and the corresponding simulated potential distribution across the device for a positive voltage applied to the ITO. (c) Voltage dependence of steady-state PL spectra for CdSe/CdS QDs (top) and InP/ZnS QDs (bottom) with an electric field of up to  $0.9 \text{ MV cm}^{-1}$ . (d) Normalized PL response under a 1 Hz AC voltage sweep (top blue). The response of both CdSe/CdS (green) and InP/ZnS (maroon) QDs, as well as a perylene diimide dye (purple) cast on the chip, mirrors the voltage sweep with minimal lag. (e) Schematic diagram of PL response of QDs in live *Xenopus laevis* retinal ganglion cell axons to cell depolarization. (f) Example traces of QD PL for CdSe and InP/ZnS following depolarization under various conditions. (g) Wide-field PL imaging of neuronal membrane depolarization using QD voltage reporters (left), where CdSe/CdS QDs are injected on top of the RGC axons expressing a calcium indicator (jGCaMP7f). Simultaneous PL of individual QDs (red) and the dye (blue) tracked in the marked locations, with the PL magnitude changes of QDs being larger than the dye during neuronal membrane depolarization (right). Reproduced from [91]. CC BY 4.0.

variations ranging from 5% to 60%. This significant difference underscores the enhanced sensitivity of QDs to changes in neuronal membrane potentials compared to traditional calcium indicator dyes commonly used as proxy voltage-sensing dyes. However, when similar experiments are conducted using InP/ZnS QDs, the results reveal some material limitations. These QDs exhibited lower brightness and rapid photobleaching, which hindered a thorough evaluation of their response. This finding emphasizes the ongoing need for material engineering improvements to optimize the performance of QDs for voltage-sensing applications. This study confirms that QDs exhibit high sensitivity to membrane depolarization, surpassing the performance of state-of-the-art calcium-based voltage imaging dyes. Their ability to track electrical events more accurately positions them as powerful tools in neuroscience research. Future integration of QDs with advanced imaging techniques, such as fast-scanning video or sheet microscopy [91], could further enhance their utility and sensitivity, paving the way for more detailed and dynamic studies of neuronal activity.

Jooken *et al* develop an artificial extracellular matrix (ECM) by engineering collagen substrates with semiconductor QDs [92]. This new method allows for the optical monitoring of the contraction activities of cardiac muscle cells. The ECM incorporates two-photon fluorescence (2PF) optical technology using QDs, representing a pioneering method for observing cellular dynamics. To evaluate the response of QDs to changes in an electric field, they constructed an apparatus to measure variations in 2PF signals under an externally applied electric field. They created a controlled electric field environment by fabricating an array of fork-shaped gold electrodes (interdigitated electrodes, IDE) with different spacings on a borosilicate glass chip and applying a potential difference across these IDEs. The chip is treated hydrophobically, and the QDs are successfully attached by dispensing them from an organic solvent and rinsing them with chloroform (CHCl<sub>3</sub>). Figure 12(a) illustrates the relationship between 2PF and changes in the electric field. The results showed that in order to achieve 2PF signal changes consistent with cellular experiments, the QDs needed to be subjected to an electric field strength of at least  $400 \text{ kV cm}^{-1}$  ( $\Delta F/F_0 = -8 \pm 2\%$ ), demonstrating sensitivity comparable to or even better than that of similar-sized I-type CdSe/ZnS QDs under single-photon illumination, thanks to the QCSE, which directly modulates the fluorescence of CdSe/ZnS QDs [92]. A patch-clamp multiphoton microscope setup is used to simultaneously measure cellular electrical activity under whole-cell current clamp conditions and the 2PF of the substrate containing QDs to detect cellular activity. Figure 12(b) shows the recording of a single-action potential via patch-clamp along with the corresponding QD 2PF trace during the rhythmic beating of cardiac cells. The sensitivity observed in these signal measurements is similar to that of recently developed voltage-sensitive dyes under two-photon illumination, with up to a 30% change in 2PF for every 100 mV change [93]. Additionally, by recording the 2PF of QDs, the beating rate and contraction-relaxation cycles of cardiac muscle cells could be monitored and quantified. The team also

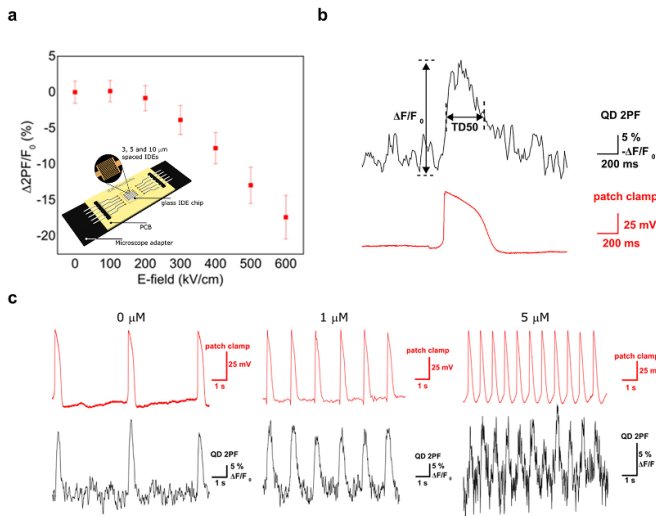


**Figure 12.** (a) Percentage change in QD 2PF as a function of the applied electric field. Inset: PCB with a central glass chip featuring gold interdigitated electrodes to apply controlled electric fields over an ensemble of QDs while measuring the 2PF. (b) Single action potential (red trace) and corresponding QD 2PF (black trace) at an expanded timescale. (c) Electrical recordings (red traces) and corresponding 2PF recordings (black traces) of drug-induced effects on cardiac contractility parameters measured by QD 2PF, which are in the absence of epinephrine, and increase in the cardiomyocyte beat rate in the presence of 1 and 5  $\mu\text{M}$  epinephrine. Reprinted with permission from [92]. Copyright (2020) American Chemical Society.

investigated the effects of adrenaline, which increased heart rate, contractile force, and relaxation rate. Figure 12(c) demonstrates the electrical activity trajectories of cardiac cells under different scenarios (exposed to adrenaline concentrations of 0, 1, and 5  $\mu\text{M}$ ), providing proof of concept for optically monitoring cardiac muscle cell activity through QD-modified collagen substrates. However, the researchers acknowledge the need for further investigation, particularly in non-contractile electrophysiological cells such as neurons. Furthermore, considering the higher temporal resolution requirements of neural activity recordings (below milliseconds), the current research has not yet met these criteria [92]. Future research may focus on improving temporal resolution and conducting more extensive studies on different cell types to achieve broader biological monitoring.

Thus, QDs hold significant promise in the realm of real-time optical voltage imaging in neuroscience. Their exceptional photoluminescent properties provide sensitivity and resilience to photobleaching, rendering them advantageous for deep-tissue imaging. Various modulation techniques, including QCSE, FRET, and PET, have been utilized to gauge electric fields and track neuronal activity using QDs. Recent research endeavors have prioritized enhancements in neuronal membrane fixation methods and surface modifications, thereby augmenting the biocompatibility of QDs. While studies have showcased the efficacy of QDs in responding membrane potential changes and monitoring cellular activity *in vivo*, visualizing instantaneous voltage changes in individual

neurons at both the single-cell and network levels remains complex and challenging, underscoring the need for further research endeavors [84].

## 5. Optical response-based electrophysiological recording with optoelectronic semiconductors

Optoelectronic semiconductors are essential components in the field of biological optical sensors. They have extensive applications across various domains. Semiconductor materials and devices, which emerged with the invention of the field-effect transistor (FET) in the late 1940s, have revolutionized electronic and photonic technologies. Advancements in device scalability, signal transduction, and remote control have led to engineering marvels like integrated circuits [94], ion-sensitive FETs [95], and optically addressable cell sensors [96]. Among these innovations, the use of inorganic semiconductors for the optical recording of biological electrical signals has gained significant attention. Inorganic semiconductors stand out for their high carrier mobility, rapid response, and sensitivity [97, 98]. They can be configured into multi-functional devices that offer desired attributes such as amplification, fast signal conduction, and low power consumption [99, 100]. This enables the precise detection of complex biological dynamics, facilitating *in-situ* biochemical and biophysical measurements, detection of molecular and cellular heterogeneity, transient biological interactions, and network-level feedback analysis [101, 102]. Inorganic semiconductor devices can also harness radiation energy and convert it into various forms, including photoelectric conversion [103, 104]. This allows the operation of miniaturized wireless devices. Examples like photovoltaic retinal implants, which use micro-sized silicon photodiodes to receive light signals and stimulate neurons, demonstrate the promising applications of inorganic semiconductors in biomedical settings. Furthermore, the ability to integrate inorganic semiconductor systems using transfer printing technology and printing photovoltaic effects expands their functionality and broadens the scope of semiconductor applications in biomedical research [105].

As neuroscience and biomedical research progress, the importance of inorganic semiconductors is increasingly recognized. Lee *et al* introduce a wireless and injectable sensing system named micro-opto-electrode (MOTE), which integrates AlGaAs micro-light-emitting diodes ( $\mu\text{LEDs}$ ) and 180 nm complementary metal-oxide-semiconductor (CMOS) circuits through heterogeneous integration [106]. Figure 13(a) illustrates that the MOTE system consists of optical and electronic components, with micrometer-scale AlGaAs diodes as both photovoltaic elements and data communication LED diodes [107, 108]. These diodes emit specific wavelengths for emission ( $\lambda_{\text{Emission}} = 825 \text{ nm}$ ) and power supply ( $\lambda_{\text{Power}} = 690 \text{ nm}$ ), optimizing photovoltaic efficiency and minimizing brain absorption [109]. Figure 13(b) shows the circuit diagram of MOTE and a SEM image of the fully released device. Figure 13(c) shows the optical response of MOTE and demonstrates the use of a 500 Hz, 500  $\mu\text{VPP}$  test signal at the input differential electrode. The signal is amplified and encoded,

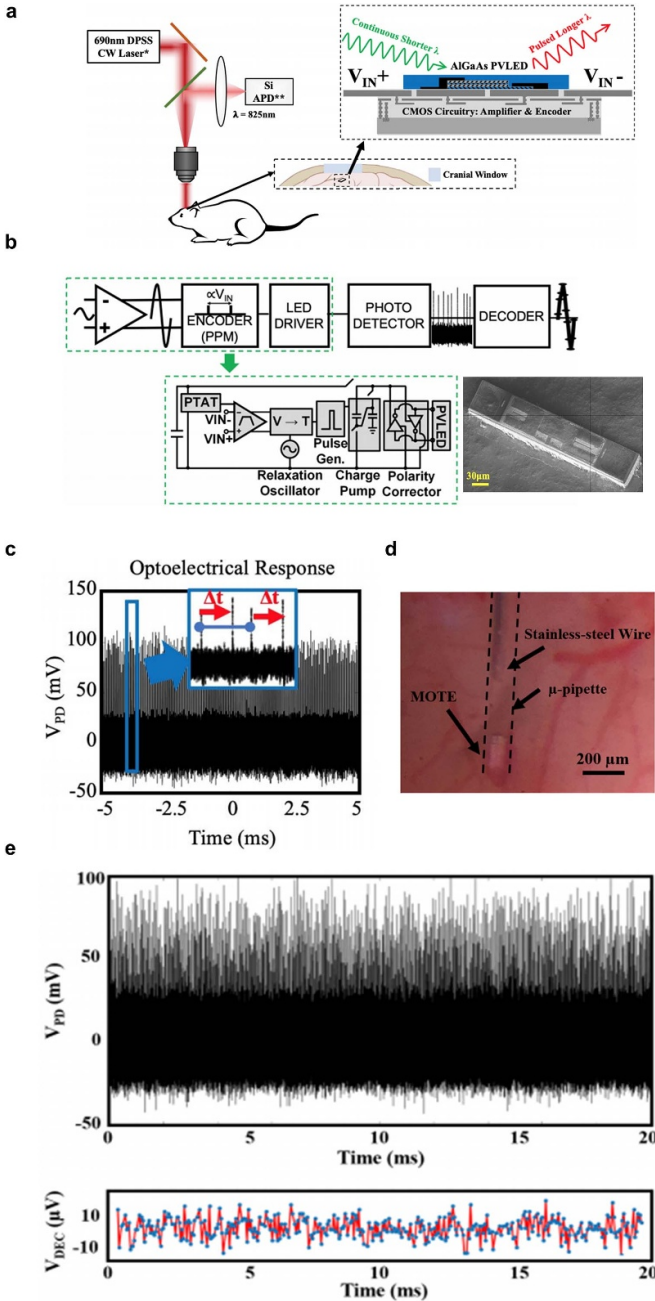


**Figure 13.** (a) Schematic diagram of a micro-scale optoelectronically transduced electrode (MOTEs) based neural recording. The inset shows that the device mainly includes an optical component for power conversion and light data communication and an electrical component for electrical signal amplification and processing. (b) system block diagram and the SEM image of a MOTE. (c) Illustration of a MOTE decoding example with a 500 Hz and 500  $\mu$ VPP signal applied at the input differential electrodes. (d) A MOTE insertion into a mouse brain using a pulled  $\mu$ -pipette. (e) *In vivo*, MOTE measurement with optical pulses (top) and decoded signal (bottom) although the inconspicuous neural response. Reproduced from [106]. CC BY 4.0.

then converted into optical pulses detected by a photodetector (PD). The time sequence of these pulses ( $\Delta t$ ) is used to reconstruct the original sinusoidal input. *In vivo* experiments are conducted to assess the insertion of MOTE into a mouse brain.

The device exhibited stable operation for over six months in saline and more than two months within the mouse brain. Figure 13(d) shows the  $\mu$ -pipette insertion method by affixing a  $\mu$ -pipette containing MOTE onto an XYZ micro-positioner with a stainless-steel wire serving as a driving mechanism. Once a skull opening is created, the  $\mu$ -pipette descends to the dura mater. MOTE, being similar in size to a razor blade, can puncture the dura mater with minimal insertion damage [106]. Although variability in insertion positions may sometimes result in the non-capture of neural signals, figure 13(e) demonstrates that MOTE can function normally and produce output pulses. This highlights the durability of heterogeneous integration as a long-term, wireless neural recording solution. The size and flexibility of the MOTE system also make it a strong contender against traditional electrode shanks and coil/ultrasound-based implants, opening up new possibilities for neuroscience research. With ongoing semiconductor device manufacturing technology advancements, miniaturization and integration have become important trends. Further miniaturization and mass production of these devices without the need for cutting or manual assembly could significantly expand their range of applications. These micro-sensor platforms, characterized by their near invisibility, cost-effectiveness, deployability in ultra-small environments, and reduced invasiveness as implantable devices, hold great promise for various applications.

As semiconductor device manufacturing technology advances, miniaturization and integration have become key trends [110–118]. Further miniaturization and scaled manufacturing processes have the potential to broaden the application domains of these devices. Cortese *et al* introduce the optical wireless integrated circuit (OWIC) platform, which integrates silicon electronic devices with inorganic micro-LEDs to create compact 100  $\mu$ m-scale packages [119]. These devices are manufactured, packaged, and released simultaneously using lithography, achieving a density of approximately 10 000 independent sensors per square inch. Figure 14(a) shows an optical image of an OWIC sensor powered remotely by a 532 nm laser, emitting light at a wavelength of 840 nm, collected through a microscope objective, and monitored using a silicon PD. Figure 14(b) illustrates the relationship between the power output of the micro-LED and the applied voltage to its input electrodes. The normalized change rate is approximately  $2.3 \times 10^{-3}$  mV $^{-1}$ , showcasing the device's precision in detecting small voltage alterations by observing the corresponding change in light output [119]. The sensor achieves a voltage resolution of  $8 \mu$ V/Hz $^{1/2}$  under continuous illumination, operates at speeds exceeding 10 kHz, and consumes about 60  $\mu$ W. By operating at a 30% duty cycle (figure 14(c)), the power consumption can be further reduced to an average of 18  $\mu$ W. Even at an average power of 1  $\mu$ W, the voltage sensitivity remains below 0.1 mV/Hz $^{1/2}$ . While this resolution suffices for numerous applications, it falls short of detecting neural activity, suggesting that future enhancements may entail more intricate circuit designs [119]. Figure 14(d) demonstrates the use of OWIC in measuring the local conductivity of sealed microfluidic channels containing water, demonstrating real-time optical recordings in a sealed polydimethylsiloxane

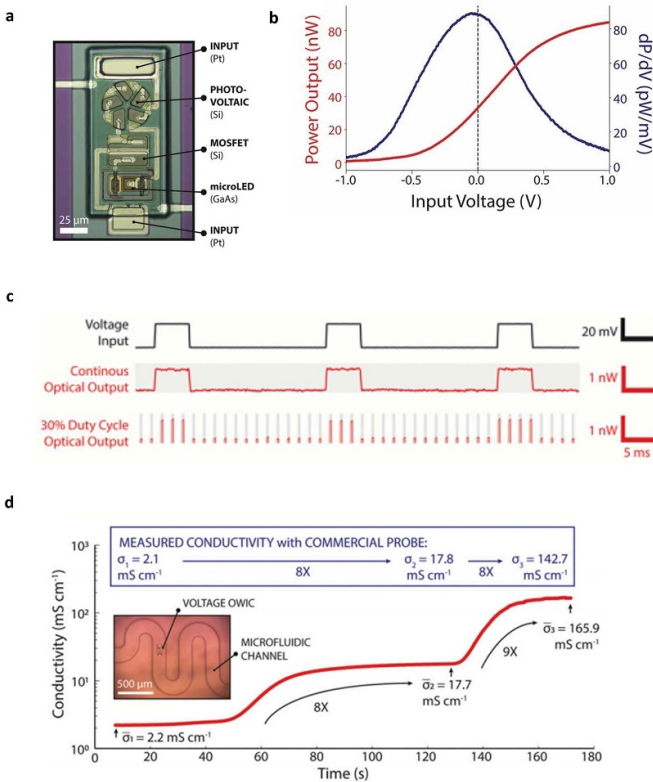


**Figure 14.** (a) Optical image of an optical wireless integrated circuits (OWIC) sensor with labeled components: input Pt electrodes, silicon photovoltaic, silicon MOSFET, and GaAs-based microLED. (b) Characteristics of optical power output as a function of voltage applied to the input electrodes. (c) A pulsed input voltage of 20 mV (black) is optically recorded by the voltage sensing OWIC (red) operating at continuous and pulsed input power. (d) Local solution conductivity in the microfluidic channel is optically recorded from a voltage-sensing OWIC and measured with a commercial probe as a reference. The insert is the optical image of the OWICs in the channel. Reproduced with permission from [119].

channel filled with a low-concentration potassium chloride (KCl) solution. The measured conductivity values closely match those obtained with commercial instruments, illustrating the efficacy of OWIC in practical settings. Furthermore, *in vivo* experiments are conducted to insert OWIC into a living mouse brain, where OWIC measures temperature with both the device and the surrounding vascular system visible. This demonstrates the promising potential of OWIC as an embedded sensor in living organisms. The OWIC platform marks a significant advancement in true microscale wireless sensors, albeit still in the first-generation and proof-of-concept stage. Expectations are high for the platform to evolve to incorporate more complex NMOS and CMOS circuits rapidly. Future research directions may encompass low-duty-cycle power schemes [119], differential radiation measurements with two different wavelength micro LEDs [120], narrow wavelength collimated vertical configurations for lower power consumption, improved communication protocols, and longer reading distances.

Furthermore, Ding *et al* introduce a heterogeneous integrated optoelectronic sensor for optically monitoring changes in bioelectric signals [121]. This sensor combines thin-film, micro-scale inorganic, and organic semiconductor devices. It incorporates gallium arsenide (GaAs)-based double-junction PDs (DJPD) with lateral dimensions of approximately  $300 \times 300 \mu\text{m}^2$ , indium gallium phosphide (InGaP) red LEDs with dimensions of about  $90 \times 90 \mu\text{m}^2$ , and organic electrochemical transistors (OECTs) based on PEDOT:PSS. The OECT features a channel length of approximately 55  $\mu\text{m}$ , a width of around 30  $\mu\text{m}$ , and a thickness of about 100 nm. The circuit concept for this sensor is depicted in figure 15(b). This sensor comprises GaAs-based DJPD and InGaP LEDs, forming an optoelectronic upconversion device. It can be excited by infrared illumination to emit red light [122]. Figure 15(c) shows multiple such devices that are serially connected to modulate an OECT channel current through variations in external gate voltage ( $V_G$ ) or changes in electrolyte concentration. Transferred on a 16  $\mu\text{m}$ -thick polyimide film substrate, the sensor includes an LED emitting red light when stimulated by infrared light. An external laser source with a wavelength of about 810 nm excites the GaAs DJPD, converting this energy into electrical power for driving the InGaP LED and the OECT. Figure 15(d) shows the simulated current-voltage curve of DJPD under an excitation intensity of  $\sim 2 \text{ W cm}^{-2}$  alongside the operational states of the LED and OECT connected in series. Notably, increasing  $V_G$  dims the red light emission from the LED, as observed by a CMOS camera (figure 15(e)). The correlation between optical output and  $V_G$ , confirmed through both measurement and calculation (figure 15(f), determination coefficient of 0.99), demonstrates high consistency. The PEDOT:PSS-based OECT structure facilitates rapid doping and undoping processes, rendering the optical signal from the integrated sensor entirely reversible under cyclic  $V_G$  applications, showcasing the potential for optical voltage sensing. To evaluate the electrical sensing capabilities, the team simulated an *in vivo* electrocardiogram (ECG) using synthetic waveforms generated by a function generator. The input signal, ranging between 10 and 100 mV peak amplitude at a frequency of 1 Hz, is applied to the gate. A fluorescence microscope monitored the changes in light intensity emitted by the sensor, submerged in a 10 mM NaCl solution with Ag/AgCl wires serving as gate electrodes (figure 15(a)). The optical readings closely matched the input voltage signals, as depicted by the 10 mV result (figure 15(g)). However, accurately capturing ECG signals, typically below 1 mV, poses challenges due to fluctuations in light emission and the limited amplification capabilities of the OECT. Further device geometry and optical configuration enhancements could improve performance. Despite these challenges, this prototype device demonstrates practical applications in wirelessly detecting bioelectric signals. Future research should focus on enhancing sensitivity for ECG recordings below 1 mV, reducing the sensor size for cellular recordings below 10  $\mu\text{m}$ , and scaling up to high-sensitivity arrays of more than 1000 channels. These advancements could significantly

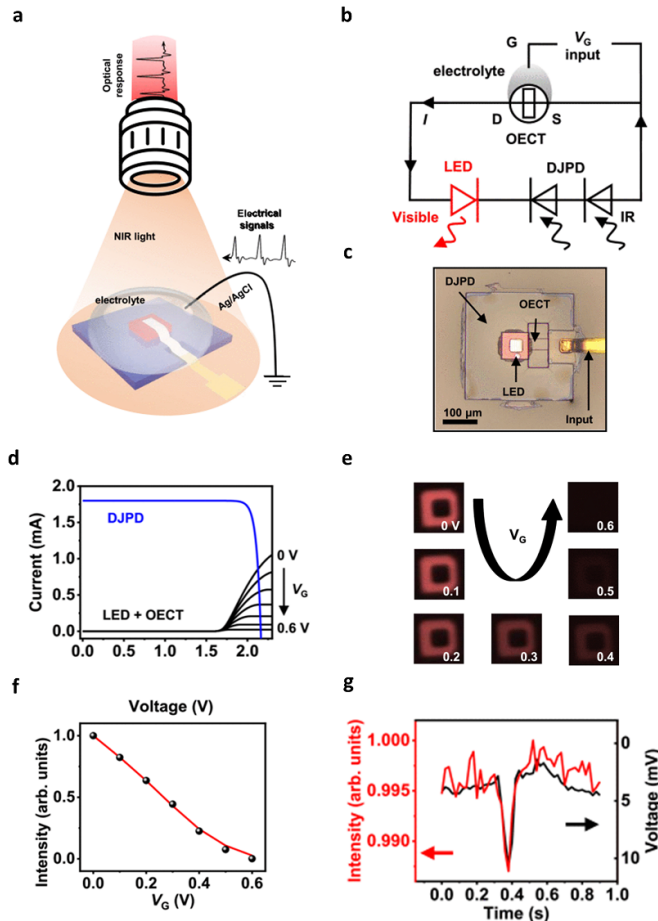


**Figure 15.** (a) Schematic diagram of optical recording of the electrical signals with heterogeneously integrated, thin-film optoelectronic device. (b) The circuit diagram (c) and optical image of the device design, including an InGaP-based red LED and a GaAs-based double junction photodiode (DYPD) connected to a PEDOT:PSS based organic electrochemical transistor (OECT). (d) Calculated current–voltage of the DYPD (red) with an excitation power density of  $\sim 2 \text{ W cm}^{-2}$  at a wavelength of  $\sim 810 \text{ nm}$ , as well as combined red LED and OECT (black) under different input gate voltages ( $V_G$ ) ranging from 0 V to 0.6 V. (e) Microscopic images of the red emission from the LED under  $V_G$  from 0 V to 0.6 V. (f) Calculated (red line) and measured (black dots) upconversion emission intensity as a function of  $V_G$ . (g) Measured luminescence changes (red) from the LED structure in response to the synthesized ECG signals (black) with a voltage of 10 mV. © (2023) IEEE. Reprinted, with permission, from [121].

expand the biomedical applications of such devices. This study presents new possibilities for integrating optoelectronic semiconductor materials and structures, underscoring the immense potential of heterogeneous integration in biomedical sensing.

Thus, advancements in optoelectronic semiconductor technology have made significant progress in the field of biomedical sensing. Researchers are integrating inorganic semiconductors to accurately record biological signals optically and developing sensor platforms like the MOTE and the OWIC to push the boundaries of sensitivity, miniaturization, and wireless functionality. The combination of inorganic and organic

semiconductor devices shows promising potential for monitoring bioelectric signals with unprecedented accuracy and versatility [123, 124]. These breakthroughs highlight the crucial role of semiconductor materials in advancing biomedical research and healthcare applications. However, challenges, including cytotoxicity [125–127], mechanical compatibility [128–130], and signal amplification [99, 100, 131] remain under investigation and improvement. With ongoing innovation and interdisciplinary collaboration, the future holds immense potential for enhancing the capabilities of optoelectronic semiconductor sensors and expanding their applications in biomedicine.

## 6. Conclusion

The optical recording of electrophysiological signals is important in neuroscience research for imaging cellular electrical activity. Table 1 summarizes recent representative advances in non-invasive monitoring optical electrophysiology, each relying on different sensing mechanisms. Electrochromic materials have a high SNR, rapid response time, and can monitor neural electrical signals without labels. Plasmonic technology provides high sensitivity and abundant photon counts by modulating signals in response to local changes in electrical potential. However, challenges such as scattering particle noise and electro-optical effects need to be addressed, along with further research on biocompatibility and safety. QD technology offers sensitivity and resolution by leveraging the properties of QDs, there is still a need to optimize the interaction between QDs and cell membranes, as well as enhance biocompatibility. Optoelectronic semiconductor methods have rapid response times, wireless functionality, and integration potential, but toxicity, compatibility with biological tissues, and signal amplification and processing improvements are necessary. These techniques have potential advantages in neuroscience, medical diagnostics, and biological research, such as rapid response, high sensitivity, label-free monitoring, and multifunctionality. However, they also face common challenges, including biocompatibility, signal processing capability, and limitations in sensitivity and resolution.

In the future, combining different optical recording techniques may optimize voltage imaging performance. However, implementing *in vivo* voltage imaging in the brain is challenging due to brain tissue scattering and weak intracellular signals being obscured by noise [132, 133]. Alternative approaches show promise, like using long-wavelength infrared illumination or near-infrared light detection with plasmonic nanoparticles and ECORE. Additionally, integrating inorganic semiconductors to enhance sensor performance and reduce power consumption may expand the application of optical recording of electrophysiological signals, improving control and imaging of neuronal activity. In conclusion, interdisciplinary collaboration and innovation are key to advancing the optical recording of electrophysiological signals for new insights into neural activity and developing diagnostic and therapeutic approaches.

**Table 1.** Recent advances in non-invasive optical recording electrophysiology.

Mechanism	Methods	Reading technique	Biological specimen	Response time	Spatial resolution	Detection limit	Year
Voltage-induced color change in electrochromic materials	ECORE	Differential detection of reflected light	Rat hippo-campal neuron/brain slice, HiPSC-derived iCMs	0.2 ms	33.4 $\mu\text{m}$	6.7 $\mu\text{V}$	2020 [39]
Plasmons interact with light, changing their physical properties	ox-PPE	Absorption spectroscopy	<i>Escherichia coli</i> , gram-positive and gram-negative strains	10 s	N/A	0.2 V	2020 [52]
Quantum dot PL response to electrophysiological signals	Plasmonic nanoantenna	Dark-field opto-electrochemical analysis	HiPSC-derived iCMs	0.2 ms	1 $\mu\text{m}$	$2 \times 10^2 \text{ V cm}^{-1}$	2019 [71]
Detection of luminescence in electrical signal modulation device	QD–Peptide–fullerene bioconjugates	Confocal laser scanning microscopy to record PL	HeLa cells, PC12 cells, primary cortical neurons	100 ms	1 $\mu\text{m}$	0.5 mV	2017 [88]
	Platform for monitoring PL response of QDs	Confocal laser scanning microscopy to record PL	Live Xenopus laevis retinal ganglion cell axons	50 ms	1 cm	$0.25 \text{ mV cm}^{-1}$	2019 [91]
	MOTE	Optical communication transmits EL signals	Mouse brain	100 $\mu\text{s}$	30 $\mu\text{m}$	N/A	2020 [107]
	Heterogeneous integration inorganic and organic semiconductor devices	EL recording by fluorescence microscopy	ECG signals	1 ms	10 $\mu\text{m}$	10 mV	2022 [123]

## Data availability statement

All data that support the findings of this study are included within the article (and any supplementary files).

## ORCID iD

He Ding  <https://orcid.org/0000-0002-0884-3112>

## Acknowledgments

H D acknowledges support by the National Natural Science Foundation of China (NSFC) (62422501), Beijing Nova Program (20230484254), Hebei Natural Science Foundation (F2024105039), and J Y acknowledges support by the National Natural Science Foundation of China (NSFC) (62101034).

## Conflict of interest

The authors declare no conflict of interest.

## References

- [1] Scanziani M and Häusser M 2009 Electrophysiology in the age of light *Nature* **461** 930–9
- [2] Hodgkin A L and Huxley A F 1939 Action potentials recorded from inside a nerve fibre *Nature* **144** 710–1
- [3] Peng S, Lacerda A E, Kirsch G E, Brown A M and Bruening-Wright A 2010 The action potential and comparative pharmacology of stem cell-derived human cardiomyocytes *J. Pharmacol. Toxicol. Methods* **61** 277–86
- [4] Sakmann B and Neher E 1984 Patch clamp techniques for studying ionic channels in excitable membranes *Annu. Rev. Phys.* **46** 455–72

- [5] Sakmann B and Neher E 1995 *Single-Channel Recording* ed B Sakmann and E Neher (Springer) pp 637–50
- [6] Kitamura K, Judkewitz B, Kano M, Denk W and Häusser M 2008 Targeted patch-clamp recordings and single-cell electroporation of unlabeled neurons *in vivo* *Nat. Methods* **5** 61–67
- [7] Kodandaramaiah S B, Franzesi G T, Chow B Y, Boyden E S and Forest C R 2012 Automated whole-cell patch-clamp electrophysiology of neurons *in vivo* *Nat. Methods* **9** 585–7
- [8] Pine J 1980 Recording action potentials from cultured neurons with extracellular microcircuit electrodes *J. Neurosci. Methods* **2** 19–31
- [9] Jones I L, Livi P, Lewandowska M K, Fiscella M, Roscic B and Hierlemann A 2011 The potential of microelectrode arrays and microelectronics for biomedical research and diagnostics *Anal. Bioanal. Chem.* **399** 2313–29
- [10] Spira M E and Hai A 2013 Multi-electrode array technologies for neuroscience and cardiology *Nat. Nanotechnol.* **8** 83–94
- [11] Xie C, Lin Z, Hanson L, Cui Y and Cui B 2012 Intracellular recording of action potentials by nanopillar electroporation *Nat. Nanotechnol.* **7** 185–90
- [12] Wilt B A, Burns L D, Wei Ho E T, Ghosh K K, Mukamel E A and Schnitzer M J 2009 Advances in light microscopy for neuroscience *Annu. Rev. Neurosci.* **32** 435–506
- [13] Peterka D S, Takahashi H and Yuste R 2011 Imaging voltage in neurons *Neuron* **69** 9–21
- [14] Valentini E, Adam E C, Karl D and Michael H 2015 All-optical interrogation of neural circuits *J. Neurosci.* **35** 13917
- [15] Tsien R Y 1980 New calcium indicators and buffers with high selectivity against magnesium and protons: design, synthesis, and properties of prototype structures *Biochemistry* **19** 2396–404
- [16] Tsien R Y 1981 A non-disruptive technique for loading calcium buffers and indicators into cells *Nature* **290** 527–8
- [17] Chen T-W *et al* 2013 Ultrasensitive fluorescent proteins for imaging neuronal activity *Nature* **499** 295–300
- [18] Miyawaki A, Llopis J, Heim R, McCaffery J M, Adams J A, Ikura M and Tsien R Y 1997 Fluorescent indicators for  $\text{Ca}^{2+}$  based on green fluorescent proteins and calmodulin *Nature* **388** 882–7
- [19] Thestrup T *et al* 2014 Optimized ratiometric calcium sensors for functional *in vivo* imaging of neurons and T lymphocytes *Nat. Methods* **11** 175–82
- [20] Tsytsarev V, Liao L-D, Kong K V, Liu Y-H, Erzurumlu R S, Olivo M and Thakor N V 2014 Recent progress in voltage-sensitive dye imaging for neuroscience *J. Nanosci. Nanotechnol.* **14** 4733–44
- [21] Kulkarni R U and Miller E W 2017 Voltage imaging: pitfalls and potential *Biochemistry* **56** 5171–7
- [22] Knöpfel T 2012 Genetically encoded optical indicators for the analysis of neuronal circuits *Nat. Rev. Neurosci.* **13** 687–700
- [23] St-Pierre F, Chavarha M and Lin M Z 2015 Designs and sensing mechanisms of genetically encoded fluorescent voltage indicators *Curr. Opin. Chem. Biol.* **27** 31–38
- [24] Lin M Z and Schnitzer M J 2016 Genetically encoded indicators of neuronal activity *Nat. Neurosci.* **19** 1142–53
- [25] Xu Y, Zou P and Cohen A E 2017 Voltage imaging with genetically encoded indicators *Curr. Opin. Chem. Biol.* **39** 1–10
- [26] Hochbaum D R *et al* 2014 All-optical electrophysiology in mammalian neurons using engineered microbial rhodopsins *Nat. Methods* **11** 825–33
- [27] Hirase H, Nikolenko V, Goldberg J H and Yuste R 2002 Multiphoton stimulation of neurons *J. Neurobiol.* **51** 237–47
- [28] Itaya K, Shibayama K, Akahoshi H and Toshima S 1982 Prussian-blue-modified electrodes: an application for a stable electrochromic display device *J. Appl. Phys.* **53** 804–5
- [29] Yamanaka K 1989 Anodically electrodeposited iridium oxide films (AEIROF) from alkaline solutions for electrochromic display devices *Jpn. J. Appl. Phys.* **28** 632
- [30] Hwang J, Tanner D B, Schwendeman I and Reynolds J R 2003 Optical properties of nondegenerate ground-state polymers: three dioxythiophene-based conjugated polymers *Phys. Rev. B* **67** 115205
- [31] Granqvist C G 2014 Electrochromics for smart windows: oxide-based thin films and devices *Thin Solid Films* **564** 1–38
- [32] Marks Z, Glugla D, Friedlein J T, Shaheen S E, McLeod R R, Kahook M Y and Nair D P 2016 Switchable diffractive optics using patterned PEDOT:PSS based electrochromic thin-films *Org. Electron.* **37** 271–9
- [33] Granqvist C G 2000 Electrochromic tungsten oxide films: review of progress 1993–1998 *Sol. Energy Mater. Sol. Cells* **60** 201–62
- [34] Cai G, Wang J and Lee P S 2016 Next-generation multifunctional electrochromic devices *Acc. Chem. Res.* **49** 1469–76
- [35] Zhou Y, Li B, Li S, Ardoña H A M, Wilson W L, Tovar J D and Schroeder C M 2017 Concentration-driven assembly and sol–gel transition of  $\pi$ -conjugated oligopeptides *ACS Cent. Sci.* **3** 986–94
- [36] Li B, Li S, Zhou Y, Ardoña H A M, Valverde L R, Wilson W L, Tovar J D and Schroeder C M 2017 Nonequilibrium self-assembly of  $\pi$ -conjugated oligopeptides in solution *ACS Appl. Mater. Interfaces* **9** 3977–84
- [37] Khodagholy D, Gelinas J N, Thesen T, Doyle W, Devinsky O, Malliaras G G and Buzsáki G 2015 NeuroGrid: recording action potentials from the surface of the brain *Nat. Neurosci.* **18** 310–5
- [38] Yu Z, Xia Y, Du D and Ouyang J 2016 PEDOT:PSS films with metallic conductivity through a treatment with common organic solutions of organic salts and their application as a transparent electrode of polymer solar cells *ACS Appl. Mater. Interfaces* **8** 11629–38
- [39] Alfonso F S *et al* 2020 Label-free optical detection of bioelectric potentials using electrochromic thin films *Proc. Natl Acad. Sci.* **117** 17260–8
- [40] Zhou Y, Liu E, Müller H and Cui B 2021 Optical electrophysiology: toward the goal of label-free voltage imaging *J. Am. Chem. Soc.* **143** 10482–99
- [41] Zhou Y, Liu E, Yang Y, Alfonso F S, Ahmed B, Nakasone K, Forró L, Müller H and Cui B 2022 Dual-color optical recording of bioelectric potentials by polymer electrochromism *J. Am. Chem. Soc.* **144** 23505–15
- [42] Moreddu R 2024 Nanotechnology and cancer bioelectricity: bridging the gap between biology and translational medicine *Adv. Sci.* **11** 2304110
- [43] Dipalo M, Amin H, Lovato L, Moia F, Caprettini V, Messina G C, Tantussi F, Berdondin L and De Angelis F 2017 Intracellular and extracellular recording of spontaneous action potentials in mammalian neurons and cardiac cells with 3D plasmonic nanoelectrodes *Nano Lett.* **17** 3932–9
- [44] Fukushima H, Katsume K, Hata Y, Kishi R and Fujiwara S 2007 Rapid separation and concentration of food-borne pathogens in food samples prior to quantification by viable-cell counting and real-time PCR *Appl. Environ. Microbiol.* **73** 92–100
- [45] Guo Q, Han J-J, Shan S, Liu D-F, Wu S-S, Xiong Y-H and Lai W-H 2016 DNA-based hybridization chain reaction and biotin-streptavidin signal amplification for sensitive

- detection of Escherichia coli O157:H7 through ELISA *Biosens. Bioelectron.* **86** 990–5
- [46] Bian X, Jing F, Li G, Fan X, Jia C, Zhou H, Jin Q and Zhao J 2015 A microfluidic droplet digital PCR for simultaneous detection of pathogenic Escherichia coli O157 and Listeria monocytogenes *Biosens. Bioelectron.* **74** 770–7
- [47] Amiri M, Bezaatpour A, Jafari H, Boukherroub R and Szunerits S 2018 Electrochemical methodologies for the detection of pathogens *ACS Sens.* **3** 1069–86
- [48] Hu F, Xu J, Zhang S, Jiang J, Yan B, Gu Y, Jiang M, Lin S and Chen S 2018 Core/shell structured halloysite/polyaniline nanotubes with enhanced electrochromic properties *J. Mater. Chem. C* **6** 5707–15
- [49] Shahrokhan S and Ranjbar S 2018 Aptamer immobilization on amino-functionalized metal–organic frameworks: an ultrasensitive platform for the electrochemical diagnostic of Escherichia coli O157:H7 *Analyst* **143** 3191–201
- [50] Zhang S, Sun G, He Y, Fu R, Gu Y and Chen S 2017 Preparation, characterization, and electrochromic properties of nanocellulose-based polyaniline nanocomposite films *ACS Appl. Mater. Interfaces* **9** 16426–34
- [51] Ranjbar S, Nejad M A F, Parolo C, Shahrokhan S and Merkoçi A 2019 Smart chip for visual detection of bacteria using the electrochromic properties of polyaniline *Anal. Chem.* **91** 14960–6
- [52] Wu J, Zhu Y, You L, Dong P-T, Mei J and Cheng J-X 2020 Polymer electrochromism driven by metabolic activity facilitates rapid and facile bacterial detection and susceptibility evaluation *Adv. Funct. Mater.* **30** 2005192
- [53] Ponder J F Jr, Österholm A M and Reynolds J R 2016 Designing a soluble PEDOT analogue without surfactants or dispersants *Macromolecules* **49** 2106–11
- [54] Ponder J F Jr, Österholm A M and Reynolds J R 2017 Conjugated polyelectrolytes as water processable precursors to aqueous compatible redox active polymers for diverse applications: electrochromism, charge storage, and biocompatible organic electronics *Chem. Mater.* **29** 4385–92
- [55] Avila-Huerta M D, Ortiz-Riaño E J, Mancera-Zapata D L and Morales-Narváez E 2020 Real-time photoluminescent biosensing based on graphene oxide-coated microplates: a rapid pathogen detection platform *Anal. Chem.* **92** 11511–5
- [56] Miranda O R, Li X, Garcia-Gonzalez L, Zhu Z-J, Yan B, Bunz U H F and Rotello V M 2011 Colorimetric bacteria sensing using a supramolecular enzyme-nanoparticle biosensor *J. Am. Chem. Soc.* **133** 9650–3
- [57] Li M, Cushing S K and Wu N 2015 Plasmon-enhanced optical sensors: a review *Analyst* **140** 386–406
- [58] Au L *et al* 2009 Effect of size, shape, composition, and support film on localized surface plasmon resonance frequency: a single particle approach applied to silver bipyramids and gold and silver nanocubes *MRS Online Proc. Libr.* **1208** 1208–O1210–1202
- [59] Ringe E, Langille M R, Sohn K, Zhang J, Huang J, Mirkin C A, Van Duyne R P and Marks L D 2012 Plasmon length: a universal parameter to describe size effects in gold nanoparticles *J. Phys. Chem. Lett.* **3** 1479–83
- [60] Jain P K and El-Sayed M A 2007 Surface plasmon resonance sensitivity of metal nanostructures: physical basis and universal scaling in metal nanoshells *J. Phys. Chem. C* **111** 17451–4
- [61] Brandl D W, Mirin N A and Nordlander P 2006 Plasmon modes of nanosphere trimers and quadruplets *J. Phys. Chem. A* **110** 12302–10
- [62] Ghosh S K and Pal T 2007 Interparticle coupling effect on the surface plasmon resonance of gold nanoparticles: from theory to applications *Chem. Rev.* **107** 4797–862
- [63] Brolo A G 2012 Plasmonics for future biosensors *Nat. Photon.* **6** 709–13
- [64] Hill R T 2015 Plasmonic biosensors *WIREs Nanomed. Nanobiotechnol.* **7** 152–68
- [65] Mauriz E 2020 Recent progress in plasmonic biosensing schemes for virus detection *Sensors* **20** 4745
- [66] Li Y, Zhao K, Sobhani H, Bao K and Nordlander P 2013 Geometric dependence of the line width of localized surface plasmon resonances *J. Phys. Chem. Lett.* **4** 1352–7
- [67] Liu X, Kang J-H, Yuan H, Park J, Kim S J, Cui Y, Hwang H Y and Brongersma M L 2017 Electrical tuning of a quantum plasmonic resonance *Nat. Nanotechnol.* **12** 866–70
- [68] Zhang J, Atay T and Nurmiikko A V 2009 Optical detection of brain cell activity using plasmonic gold nanoparticles *Nano Lett.* **9** 519–24
- [69] McIntyre J D E 1973 Electrochemical modulation spectroscopy *Surf. Sci.* **37** 658–82
- [70] Lioubimov V, Kolomenskii A, Mershin A, Nanopoulos D V and Schuessler H A 2004 Effect of varying electric potential on surface-plasmon resonance sensing *Appl. Opt.* **43** 3426–32
- [71] Habib A, Zhu X, Can U I, McLanahan M L, Zorlutuna P and Yanik A A 2019 Electro-plasmonic nanoantenna: a nonfluorescent optical probe for ultrasensitive label-free detection of electrophysiological signals *Sci. Adv.* **5** eaav9786
- [72] Alù A and Engheta N 2008 Input impedance, nanocircuit loading, and radiation tuning of optical nanoantennas *Phys. Rev. Lett.* **101** 043901
- [73] Engheta N 2007 Circuits with light at nanoscales: optical nanocircuits inspired by metamaterials *Science* **317** 1698–702
- [74] Marx V 2014 Neurobiology: rethinking the electrode *Nat. Methods* **11** 1099–103
- [75] Obien M E J, Deligkaris K, Bullmann T, Bakkum D J and Frey U 2015 Revealing neuronal function through microelectrode array recordings *Front. Neurosci.* **8** 423
- [76] Musk E 2019 An integrated brain-machine interface platform with thousands of channels *J. Med. Internet Res.* **21** e16194
- [77] Hardy N, Habib A, Ivanov T and Yanik A A 2021 Neuro-SWARM<sup>3</sup>: system-on-a-nanoparticle for wireless recording of brain activity *IEEE Photonics Technol Lett.* **33** 900–3
- [78] Liao K, Yang Z, Tao D, Zhao L, Pires N, Dorao C A, Stokke B T, Roseng L E, Liu W and Jiang Z 2024 Exploring the intersection of brain–computer interfaces and quantum sensing: a review of research progress and future trends *Adv. Quantum Technol.* **7** 2300185
- [79] Rowland C E *et al* 2015 Electric field modulation of semiconductor quantum dot photoluminescence: insights into the design of robust voltage-sensitive cellular imaging probes *Nano Lett.* **15** 6848–54
- [80] Walters R *et al* 2012 Nanoparticle targeting to neurons in a rat hippocampal slice culture model *ASN Neuro* **4** 383–392
- [81] Bradburne C E, Delehanty J B, Boeneman Gemmill K, Mei B C, Matoussi H, Susumu K, Blanco-Canosa J B, Dawson P E and Medintz I L 2013 Cytotoxicity of quantum dots used for *in vitro* cellular labeling: role of QD surface ligand, delivery modality, cell type, and direct comparison to organic fluorophores *Bioconjugate Chem.* **24** 1570–83
- [82] Agarwal R *et al* 2015 Delivery and tracking of quantum dot peptide bioconjugates in an intact developing avian brain *ACS Chem. Neurosci.* **6** 494–504
- [83] Chen Y, Vela J, Htoon H, Casson J L, Werder D J, Bussian D A, Klimov V I and Hollingsworth J A 2008

- “Giant” multishell CdSe nanocrystal quantum dots with suppressed blinking *J. Am. Chem. Soc.* **130** 5026–7
- [84] Efros A L *et al* 2018 Evaluating the potential of using quantum dots for monitoring electrical signals in neurons *Nat. Nanotechnol.* **13** 278–88
- [85] Ansari A A, Thakur V K and Chen G 2021 Functionalized upconversion nanoparticles: new strategy towards FRET-based luminescence bio-sensing *Coord. Chem. Rev.* **436** 213821
- [86] Imani M, Mohajeri N, Rastegar M and Zarghami N 2021 Recent advances in FRET-based biosensors for biomedical applications *Anal. Biochem.* **630** 114323
- [87] Miller E W, Lin J Y, Frady E P, Steinbach P A, Kristan W B and Tsien R Y 2012 Optically monitoring voltage in neurons by photo-induced electron transfer through molecular wires *Proc. Natl Acad. Sci. USA* **109** 2114–9
- [88] Nag O K *et al* 2017 Quantum dot-peptide-fullerene bioconjugates for visualization of *in vitro* and *in vivo* cellular membrane potential *ACS Nano* **11** 5598–613
- [89] Tsytsovarev V, Premachandra K, Takeshita D and Bahar S 2008 Imaging cortical electrical stimulation *in vivo*: fast intrinsic optical signal versus voltage-sensitive dyes *Opt. Lett.* **33** 1032–4
- [90] Bezanilla F 2008 How membrane proteins sense voltage *Nat. Rev. Mol. Cell Biol.* **9** 323–32
- [91] Caglar M, Pandya R, Xiao J, Foster S K, Divitini G, Chen R Y S, Greenham N C, Franze K, Rao A and Keyser U F 2019 All-optical detection of neuronal membrane depolarization in live cells using colloidal quantum dots *Nano Lett.* **19** 8539–49
- [92] Jokken S *et al* 2020 Quantum dot-functionalized extracellular matrices for *in situ* monitoring of cardiomyocyte activity *ACS Appl. Nano Mater.* **3** 6118–26
- [93] Park K, Deutsch Z, Li J J, Oron D and Weiss S 2012 Single molecule quantum-confined stark effect measurements of semiconductor nanoparticles at room temperature *ACS Nano* **6** 10013–23
- [94] Jiang Y and Tian B 2018 Inorganic semiconductor biointerfaces *Nat. Rev. Mater.* **3** 473–90
- [95] Ma X, Peng R, Mao W, Lin Y and Yu H 2023 Recent advances in ion-sensitive field-effect transistors for biosensing applications *Electrochim. Sci. Adv.* **3** e2100163
- [96] Meng Y, Chen F, Wu C, Krause S, Wang J and Zhang D-W 2022 Light-addressable electrochemical sensors toward spatially resolved biosensing and imaging applications *ACS Sens.* **7** 1791–807
- [97] Rivnay J, Inal S, Collins B A, Sessolo M, Stavrinidou E, Strakosas X, Tassone C, Delongchamp D M and Malliaras G G 2016 Structural control of mixed ionic and electronic transport in conducting polymers *Nat. Commun.* **7** 11287
- [98] Xu J *et al* 2017 Highly stretchable polymer semiconductor films through the nanoconfinement effect *Science* **355** 59–64
- [99] Lutz J, Schlangenotto H, Scheuermann U and De Doncker R 2018 Semiconductor properties *Physical Characterization and Reliability* vol 2, ed J Lutz (Springer) pp 21–99
- [100] Sze S M, Li Y and Ng K K 2021 *Physics of Semiconductor Devices* (Wiley)
- [101] Strukov D B and Likharev K K 2007 Defect-tolerant architectures for nanoelectronic crossbar memories *J. Nanosci. Nanotechnol.* **7** 151–67
- [102] Mathieson K *et al* 2012 Photovoltaic retinal prosthesis with high pixel density *Nat. Photon.* **6** 391–7
- [103] Jiang Y *et al* 2018 Rational design of silicon structures for optically controlled multiscale biointerfaces *Nat. Biomed. Eng.* **2** 508–21
- [104] Loudin J D, Cogan S F, Mathieson K, Sher A and Palanker D V 2011 Photodiode circuits for retinal prostheses *IEEE Trans. Biomed. Circuits Syst.* **5** 468–80
- [105] Narvaez J, Vasquez-Sancho F and Catalan G 2016 Enhanced flexoelectric-like response in oxide semiconductors *Nature* **538** 219–21
- [106] Lee S *et al* 2020 Fabrication of injectable micro-scale opto-electronically transduced electrodes (MOTES) for physiological monitoring *J. Microelectromech. Syst.* **29** 720–6
- [107] Haydaroglu I and Mutlu S 2014 Optical power delivery and data transmission in a wireless and batteryless microsystem using a single light emitting diode *J. Microelectromech. Syst.* **24** 155–65
- [108] Haydaroglu I, Ozgun M T and Mutlu S 2017 Optically powered optical transmitter using a single light-emitting diode *IEEE Trans. Circuits Syst. I* **64** 2003–12
- [109] Podgorski K and Ranganathan G 2016 Brain heating induced by near-infrared lasers during multiphoton microscopy *J. Neurophysiol.* **116** 1012–23
- [110] Warneke B, Last M, Liebowitz B and Pister K S 2001 Smart dust: communicating with a cubic-millimeter computer *Computer* **34** 44–51
- [111] Biederman W *et al* 2013 A fully-integrated, miniaturized ( $0.125 \text{ mm}^2$ )  $10.5 \mu\text{W}$  wireless neural sensor *IEEE J. Solid-State Circuits* **48** 960–70
- [112] Chen G *et al* 2011 *IEEE Int. Solid-State Circuits Conf.* (IEEE) pp 310–2
- [113] Harrison R R *et al* 2006 A low-power integrated circuit for a wireless 100-electrode neural recording system *IEEE J. Solid-State Circuits* **42** 123–33
- [114] Ho J S, Yeh A J, Neofytou E, Kim S, Tanabe Y, Patlolla B, Beygui R E and Poon A S Y 2014 Wireless power transfer to deep-tissue microimplants *Proc. Natl Acad. Sci. USA* **111** 7974–9
- [115] Jeong S *et al* 2014 A fully-integrated 71 nW CMOS temperature sensor for low power wireless sensor nodes *IEEE J. Solid-State Circuits* **49** 1682–93
- [116] Yeon P, Mirbozorgi S A, Ash B, Eckhardt H and Ghovanloo M 2016 Fabrication and microassembly of a mm-sized floating probe for a distributed wireless neural interface *Micromachines* **7** 154
- [117] Seo D, Neely R M, Shen K, Singhal U, Alon E, Rabaey J M, Carmena J M and Mahabir M M 2016 Wireless recording in the peripheral nervous system with ultrasonic neural dust *Neuron* **91** 529–39
- [118] Lee S, Cortese A J, Gandhi A P, Agger E R, McEuen P L and Molnar A C 2018 A  $250 \mu\text{m} \times 57 \mu\text{m}$  microscale opto-electronically transduced electrodes (MOTES) for neural recording *IEEE Trans. Biomed. Circuits Syst.* **12** 1256–66
- [119] Cortese A J *et al* 2020 Microscopic sensors using optical wireless integrated circuits *Proc. Natl Acad. Sci. USA* **117** 9173–9
- [120] Guo X, Mandelis A and Zinman B 2012 Noninvasive glucose detection in human skin using wavelength modulated differential laser photothermal radiometry *Biomed. Opt. Express* **3** 3012–21
- [121] Ding H *et al* 2023 Heterogeneous integration of thin-film organic and inorganic devices for optical based bioelectrical and chemical sensing *IEEE J. Sel. Top. Quantum Electron.* **29** 1–20
- [122] Ding H *et al* 2018 Microscale optoelectronic infrared-to-visible upconversion devices and their use as injectable light sources *Proc. Natl Acad. Sci.* **115** 6632–7
- [123] Kang S-K *et al* 2016 Bioresorbable silicon electronic sensors for the brain *Nature* **530** 71–76

- [124] Kim D-H, Ahn J-H, Choi W M, Kim H-S, Kim T-H, Song J, Huang Y Y, Liu Z, Lu C and Rogers J A 2008 Stretchable and foldable silicon integrated circuits *Science* **320** 507–11
- [125] Srivastava V, Gusain D and Sharma Y C 2015 Critical review on the toxicity of some widely used engineered nanoparticles *Ind. Eng. Chem. Res.* **54** 6209–33
- [126] Wu Y-L *et al* 2013 Biophysical responses upon the interaction of nanomaterials with cellular interfaces *Acc. Chem. Res.* **46** 782–91
- [127] Reiss P, Carriere M, Lincheneau C, Vaure L and Tamang S 2016 Synthesis of semiconductor nanocrystals, focusing on nontoxic and earth-abundant materials *Chem. Rev.* **116** 10731–819
- [128] Lacour S P, Courtine G and Guck J 2016 Materials and technologies for soft implantable neuroprostheses *Nat. Rev. Mater.* **1** 1–14
- [129] Salatino J W, Ludwig K A, Kozai T D and Purcell E K 2017 Glial responses to implanted electrodes in the brain *Nat. Biomed. Eng.* **1** 862–77
- [130] Chen R, Canales A and Anikeeva P 2017 Neural recording and modulation technologies *Nat. Rev. Mater.* **2** 1–16
- [131] Pierret R F 1996 *Semiconductor Device Fundamentals* (Pearson Education India)
- [132] Witte S, Negrean A, Lodder J C, de Kock C P J, Testa Silva G, Mansvelder H D and Louise Groot M 2011 Label-free live brain imaging and targeted patching with third-harmonic generation microscopy *Proc. Natl Acad. Sci. USA* **108** 5970–5
- [133] Liu R, Zhao S and Liu J 2020 From lithographically patternable to genetically patternable electronic materials for miniaturized, scalable, and soft implantable bioelectronics to interface with nervous and cardiac systems *ACS Appl. Electron. Mater.* **3** 101–18